Research Square

Preprints are preliminary reports that have not undergone peer review.
They should not be considered conclusive, used to inform clinical practice,
or referenced by the media as validated information.

Forward and inverse prediction of micro-channel topographies in abrasive slurry jet machining: a machine learning framework and a graphical web-based tool

Majid Moghaddam

majid.moghaddam@torontomu.ca

Toronto Metropolitan University https://orcid.org/0000-0002-5647-9415

Fatemeh Safaei

Marcello Papini

Research Article

Keywords: machine learning, abrasive slurry jet, artificial neural network, random forest, deep learning, inverse methods

Posted Date: July 3rd, 2026

DOI: https://doi.org/10.21203/rs.3.rs-10167346/v1

License: This work is licensed under a Creative Commons Attribution 4.0 International License.
Read Full License

Version of Record: A version of this preprint was published at The International Journal of Advanced Manufacturing Technology on September 30th, 2026. See the published version at https://doi.org/10.1007/s00170-026-19169-0.

Forward and inverse prediction of micro-channel topographies in abrasive slurry jet machining: a machine learning framework and a graphical web-based tool

Majid Moghaddam a*, Fatemeh Safaei b, Marcello Papini a*

[a] *Department of Mechanical, Industrial, and Mechatronics Engineering, Toronto Metropolitan University, 350 Victoria Street, Toronto, ON, M5B 2K3, Canada*

[b] *Technology department, Moneris Solutions, 195 The West Mall, Etobicoke, ON, M9C 5K1, Canada*

Abstract

Abrasive slurry jet micro-machining (ASJM) is one of very few processes able to sculpt high-aspect-ratio micro-features in hard, brittle, or temperature-sensitive materials at low cost and without a heat-affected zone, making it strategically important for biomedical microfluidic devices, MEMS, micro-mould cavities, and aerospace cooling-channel manufacturing. However, its industrial uptake remains constrained by the difficulty in predicting and controlling the machined topography. Abrasive slurry jets can be used as cost-effective means for micro-milling virtually any material. However, they have been criticized for the difficulties associated with their predictability and control. The large number of parameters affecting the machining topography and the nonlinear flow dynamics and particle erosion during the process makes the forward problem, i.e., prediction of the eroded topography, extremely difficult. The even more difficult inverse problem, i.e. determining the operating conditions to machine a desired topography, has rarely been considered. This paper aims to use machine learning as a versatile and computationally efficient technique to address both the forward and inverse challenges when using abrasive slurry jets to micro-machine channels in AA6061-T6. Traditional machine learning models such as polynomial regression and random forest, as well as deep learning models such as artificial neural networks (ANN) and convolutional neural networks (CNN), were trained and their accuracy and robustness for the forward prediction of the machined surface profiles were compared. The effect of dataset size on the accuracy of models was also studied. A full factorial design of experiments was used to collect training data at various pressures, feed rates, standoff distances, and numbers of machining passes. All forward models successfully predicted micro-channel profiles spanning aspect ratios from 0.06 to ~2, achieving coefficients of determination (R^2) of 0.76–0.82, mean absolute errors (MAE) of 0.003–0.005 mm, and mean squared errors (MSE) below 0.00013 mm^2. For inverse prediction, an ANN was trained to infer process parameters for a target geometry, achieving R^2 values of 0.55–0.94, MAE of 0.015–0.034 mm, and MSE of 0.00067–0.002 mm^2. These results demonstrate that ML enables efficient and accurate prediction of both machined profiles and the required operating parameters, highlighting its strong potential to enhance process planning and real-time control in abrasive slurry jet micro-machining. The trained models are also packaged as a free web application so that ASJM operators without programming experience can use them in a browser (https://asjm-channel-predictor.streamlit.app/).

Keywords: machine learning; abrasive slurry jet; artificial neural network; random forest; deep learning; inverse methods

*Corresponding authors.
E-mail address: majid.moghaddam@torontomu.ca (M. Moghaddam),
mpapini@torontomu.ca (M. Papini)

1. Introduction

Abrasive water (AWJ) and slurry jets (ASJ) can be used to micro-machine surfaces as an alternative to conventional machine tools, laser etching [1], electro-discharge machining (EDM) [2], and electrochemical milling (ECM) [3]. The technology offers notable advantages, including material versatility, minimal cutting forces, no heat affected zone, environmental friendliness, and low cost. For micro-feature applications in particular, ASJM offers a unique combination of capabilities: it can machine virtually any material (metals, ceramics, glass, polymers, composites) at characteristic feature sizes below 200 μm, at a fraction of the capital and operating cost of laser, EDM, or ECM equipment, and without introducing thermal damage that would compromise downstream functional surfaces. Unlocking accurate, deployable predictive models for ASJM therefore directly enables manufacturing routes for product classes, implantable microfluidic chips, biocompatible MEMS, and free-form micro-cooling channels in turbine components, where competing micro-machining technologies are either prohibited or uneconomical. [4,5].

Abrasive slurry jet machining (ASJM) uses a jet of water carrying high speed micron-sized particles to gradually etch the surface. Despite their unique advantages, several factors make the eroded topography in ASJM challenging to predict. Some of these factors include:

(i) **High turbulence of the jet and the complexity of its flow dynamics.** Upon impingement, a pressurized stagnation zone forms in the jet near the surface, altering the distribution of erosive potential from that upstream. The zone can become asymmetric and irregular depending on the surface topography which continuously changes during the process. Additionally, recirculation zones may develop, further altering jet dynamics [6].

(ii) **Nonlinear nature of solid particle erosion.** Particles erode the surface at varying rates depending on their impact angle, velocity, and local flux. The particle velocity and flux are distributed nonuniformly with the jet, and the fluid's complex dynamics make particle trajectories difficult to predict. Secondary strikes of

particles, driven by the lateral flow within the eroded feature, add further complication [7,8].

(iii) **Multitude of operating parameters.** Pump pressure, nozzle traverse speed, abrasive flow rate, standoff distance (SOD), abrasive size, sphericity, and hardness, target surface hardness, angle of attack, number of passes, and the degree of overlap between raster scans are among the parameters that affect the eroded topography. Some of these parameters are interdependent, making prediction of a global relationship between the process inputs and outputs very difficult [9].

Several semi-empirical, analytical, numerical, and stochastic techniques have been developed to predict the milled surface topography or determine the inverse kinematics of the abrasive jet machine. For instance, Axinte et al. [10] developed a geometrical model based on nonlinear partial differential equations to predict AWJ channel profiles. Their model relies on the material's specific etch rate, calibrated using the profile of a shallow channel, for accurate prediction of channel profiles at virtually any feed rate. However, their model does not consider the impact angle dependency of the erosion and is thus only appropriate for shallow features machined using only one pass at perpendicular jet incidence. Complementing Axinte et al.'s model, Kong et al. [11] developed a geometrical model that accounts for the distribution of impact angles across the jet. This model also relies on the specific etch rate distribution, derived from a shallow profile, to predict channel topographies under arbitrary conditions. Despite being more versatile than previous geometrical models, it is not expected to provide accurate predictions for multi-pass milling scenarios that result in high aspect ratio features where steeper sidewall slopes can affect the local particle impact angles, and thus the local etch rate.

To allow for the prediction of higher aspect ratio features machined using ASJM, more recent work has focused on using computational fluid dynamics (CFD) to predict the local erosion rates within the evolving eroded topography. For example, Moghaddam et al. [12] recently used CFD modeling coupled with Lagrangian particle tracing and surface evolution modeling to gain detailed insights into the changes in process mechanisms such as stagnation zone development and localized erosion that occur as the machined feature develops. They further developed this method to predict the surface evolution of features milled using overlapping masked and unmasked ASJM [6,13].

Despite their high fidelity, the main limitations of the existing numerical modeling-based techniques is their high computational cost, and the difficulty in inverting them to predict inputs from outcomes. To solve the forward problem, at each machining pass, the fluid dynamics must

first be solved, then the particle trajectories calculated, and finally the geometry updated, and the process repeated for each subsequent pass. They are thus mostly useful for providing insights into the physics of the machining process and applying them in industrial applications where real-time predictions are required is difficult.

Statistical and data-driven techniques such as machine learning (ML) have shown great promise in accelerated predictions of abrasive jet machining outcomes such as surface quality. Ramesh and Mani [14] used ε-support vector regression and quadratic regression models to predict the effect of AWJ parameters on the surface roughness of planar surfaces milled on alumina ceramics which allowed them identify the optimal parameters for minimum roughness. Ćojbašić et al. [15] used the extreme learning machine (ELM) method to predict the surface roughness for the AWJM of aluminum alloy based on key machining parameters such feed rate, material thickness, abrasive flow rate, and measurement position. They reported that ELM outperformed ANN and genetic programming (GP) in predicative accuracy. However, they did not model the effect of water pressure which can be a major determinant in surface roughness.

Nag et al. [16] used random forest and support vector machines for the prediction and classification of erosion characteristics due to repetitive impact of pulsating water jets on 6060 aluminum alloy and AISI 304 stainless steel. They reported accurate ML predictions of the crater volumes eroded under various conditions. Mogul et al. [17] used a back propagation neural network (BpNN) algorithm to predict the depth of cut in the AWJM of Ti-6Al-4V aluminum alloy for varying water pressures, feed rates, abrasive mass flow rates, orifice sizes, and nozzle to orifice diameter ratios. They reported that the BpNN model performed well for moderate and large depth cuts (> 6 mm), but that the accuracy decreased sharply at low depths, with deviations exceeding 200% in some cases. They did not predict the kerf profiles, and their study was limited to quantitative predictions of depth.

Ramesha et al. [18] compared Response Surface Methodology (RSM), ANN, RF, and Extreme Gradient Boosting (XGBoost) to predict the optimize material removal rate, kerf widths, and surface roughnesses during submerged AWJ suspension machining of carbon fiber-reinforced polymer composites. They found that, although all the models could reasonably predict the experimental results and capture the non-linear relationships, XGBoost and ANN outperformed RSM and RF in both accuracy and generalization. They also found that the stand off distance (SOD) had the most significant effect on the material removal rate and surface roughness. Since their dataset was limited to only 9 experiments, the reliability and general applicability of the ML models was limited.

Prabhu and Kanthababu [19] predicted the surface roughness and depth of cut for the AWJM of alumina ceramic by developing ML models trained on a small experimental dataset including only 29 runs. To compensate for the limited data, they applied bootstrapping-based data augmentation and compared the predictive performance of Multilayer Perceptron (MLP), Decision Tree, and RF regressors, with hyperparameter tuning. They reported that the MLP model showed superior performance in predicting the surface roughness, while the Random Forest model was most effective for depth of cut. Their study effectively highlights the potential of combining machine learning with data augmentation in non-traditional machining. However, since the original dataset was limited, the reliance on synthetic samples may not fully capture the variability of real-world conditions. Including external validation and additional discussion on model interpretability could further strengthen the reliability and practical impact of the approach.

All of the above ML-based methods were limited to predicting surface quality. None attempted to predict the full eroded surface profile, much less consider the more difficult inverse problem of determining the process parameters to sculpt a desired topography. Although useful literature can be found for the analogous problem in additive manufacturing, where inverse problems using ML frameworks [20] like those proposed in this work have been used effectively, inverse modeling for abrasive jet machining has been limited. If the desired shape is relatively flat (low AR), the eroded depth at any point depends linearly on the 'erosive efficacy' (product of particle mass flux and velocity). In this case, for air-driven abrasive jet machining, the nozzle scan speed variation needed to create a micro-channel with a desired texture along its length can be directly determined [21]. For higher ARs, the optimal combination of adjacent raster scan speeds and positions to create a limited set of desired channel shapes can be determined by iterating a SE model [22]. For AWJM, more complex adjoint optimization schemes [23] have been proposed to determine the raster speeds and paths needed to create prescribed shallow but complex patterns. These schemes, however, fail at higher ARs because they neglect critical physics such as secondary slurry flow and etch rate changes on the sloped sidewalls.

1.1. Scope of the present work

As discussed above, controlled depth milling using abrasive jets is challenging and requires accurate predictive modeling. The prediction of the machined topography (i.e., the forward problem) is primarily limited to analytical and numerical approaches, where the former often lacks accuracy, and the latter tends to be computationally expensive. On the other hand, ML-

based techniques have thus far been used only for predictions of single machining outputs such as the surface roughness, depth of cut, or material removal rate. Neither approach has considered the inverse problem for deeper, higher aspect ratio features.

The present study is a pioneering effort to assess the applicability of ML approaches to both forward and inverse ASJ machined topography problems. As an example, to establish feasibility, the prediction of the surface evolution of micro-channels machined into Al 6061-T6 alloy using multiple jet passes is considered. The predictions are made for a wide variety SODs, pressures, traverse speeds, and number of passes producing channels having a wide range of aspect ratios. A full factorial design of experiments consisting of 270 runs is used to collect a relatively large database for model training, validation, and testing. The performance of various models such as nonlinear regression, random forest, artificial neural networks and one-dimensional convolutional neural networks is evaluated by comparing their mean squared error (MSE), mean absolute error (MAE), and the coefficient of determination (R^2). Furthermore, the sensitivity of models' performance on the size of databases is studied. Finally, the forward model is inverted, i.e., to determine the process parameters required to produce a micro-channel of a given desired topography. To make the trained models practically usable, both the forward predictor and the inverse search have been deployed as a free web application that runs in any browser (https://asjm-channel-predictor.streamlit.app/) and returns ranked feasible recipes for a target geometry.

The specific contributions of this work are: (i) the first ML framework that predicts the full vector-valued cross-sectional profile of ASJM-machined micro-channels, rather than scalar quantities such as roughness or depth of cut as in prior ASJM-ML studies; (ii) a physics-informed feature set and monotonicity-aware training scheme that encodes known erosion-rate dependencies (cumulative erosive potential P×N, exposure SOD×V, and erosive intensity per unit traverse P/V) consistently across all forward models, ensuring a fair comparison; (iii) a probabilistic, constraint-aware inverse design framework that explicitly addresses the many-to-one nature of the inverse problem by returning a set of feasible parameter combinations together with an uncertainty estimate, rather than a single deterministic guess; and (iv) a quantitative assessment of real-time applicability (per-sample inference latency on a CPU) and noise robustness, demonstrating that the surrogates are deployable as the predictive core of a closed-loop process-control system. Finally, (v) the trained model, the inverse search and the experimental dataset are released as a public web application (https://asjm-channel-

predictor.streamlit.app/), so that other ASJM users can try the methodology on their own targets without writing any code.

2. Experiments and data collection

Micro-channel machining experiments were performed under various operating parameters to provide learning, validation, and testing datasets for the ML models. AA6061-T6 aluminum with a Vickers hardness and density of 0.98 GPa and 2700 kg/m^3, respectively, was machined using garnet abrasives (Barton International, Glens Falls, NY, USA) with average equivalent diameter of 33.6 μm (±4.03 μm standard deviation) and average sphericity of 0.41 (±0.12 μ standard deviation). This particle/target system has been previously shown to exhibit the ductile erosion that is typical of many metal target systems [6]. Since ductile systems are highly sensitive to the impact angles of the abrasives, they are more complex to model than the simpler brittle erosive systems which only depend on the perpendicular component of the impact angle [24,25].

The independent variables included water pressure, P, nozzle traverse speed, V, standoff distance, SOD, and the number of machining passes, N, which were varied in the ranges shown in Table 1. The operating parameters were selected based on the limits of the OMAX machine to mill micro-channels at a relatively wide range of aspect ratios. Fig. 1a shows the schematics of a channel milled on the substrate, indicating the SOD and traverse direction. Multi-pass channels were machined by traversing the jet repeatedly over the previously milled channels. Fig. 1b schematically shows the evolution of the cross-sectional profiles of typical multi-pass channels. A full factorial design of experiments (DOE) was used to provide a comprehensive dataset for the model training, leading to $3 \times 3 \times 3 \times 10 = 270$ combinations of operating parameters. Each test was repeated three times, making the total number of tests 810.

A high-pressure ASJM setup with schematics shown in Fig. 1a was used to mill micro-channels which modified an OMAX 2626 jet machining center (OMAX Corp., Kent, Washington, USA) by replacing the dry abrasive hopper with a slurry tank containing an aqueous slurry with 10 wt% abrasives, constantly stirred using a mixer with 1000 rpm, providing steady concentration, and preventing particle sediment. The ASJM setup eliminates the entrained air from the jet mixture, reducing its footprint size with the added advantage of reduced roughness and waviness compared to AWJM [26]. The slurry tank was placed 1 m above the nozzle and a plastic hose with 1.27 mm^2 cross-sectional area was connected to the mixing tube to ensure maximum flow rate without the risk of the nozzle clogging or the mixing

tube flooding [27]. The apparatus was fitted with a micro-nozzle having orifice and mixing tube diameters of 127 μm and 254 μm, respectively. As shown in Fig. 1c, the nozzle was computer controlled in *x*, *y*, and *z* directions with a positional accuracy of 76 μm over a course of 30 cm at a maximum traverse speed of 4572 mm/min.

A stepped path strategy was used to mill the multi-pass channels. As explained in other works [6,13], this involved machining the first pass along a 15 cm length, after which subsequent passes machined over the channel used ever-decreasing traverse lengths. In this manner, the experiments could be performed continuously without interrupting the flow of slurry, while preserving 1.5 cm long portions of the machined surface corresponding to each pass, and thus recording the surface evolution history. ~1500 cross-sectional profiles were measured along each channel's length using a 3D optical profilometer (S-neox, Sensofar Surface Metrology Inc., Barcelona, Spain). For each case, a representative cross-sectional profile was chosen as the one closest to the average among the three tests, and exported as a series of *x* and *z* coordinates. These (x, z) coordinates were used for model training and validation, as will be described in Section 3. The experimental dataset is provided in the supplementary materials.

Table 1. Experimental specifications used for data collections.

Parameter	**Value**
Pump pressure, *P* (MPa)	193, 234. 275
Jet centerline velocity (m/s) [12]	230.2, 248.8, 267.3
Slurry mass flow rate (g/min) [12]	56.5, 184.2, 192.4
Feed rate, *V* (mm/min)	500, 1000, 1500
SOD (mm)	1, 3, 5
Number of passes, *N*	1, 2, …, 10
Global angle of attack (°)	90
Nozzle orifice diameter (μm)	127
Mixing tube diameter (μm)	254

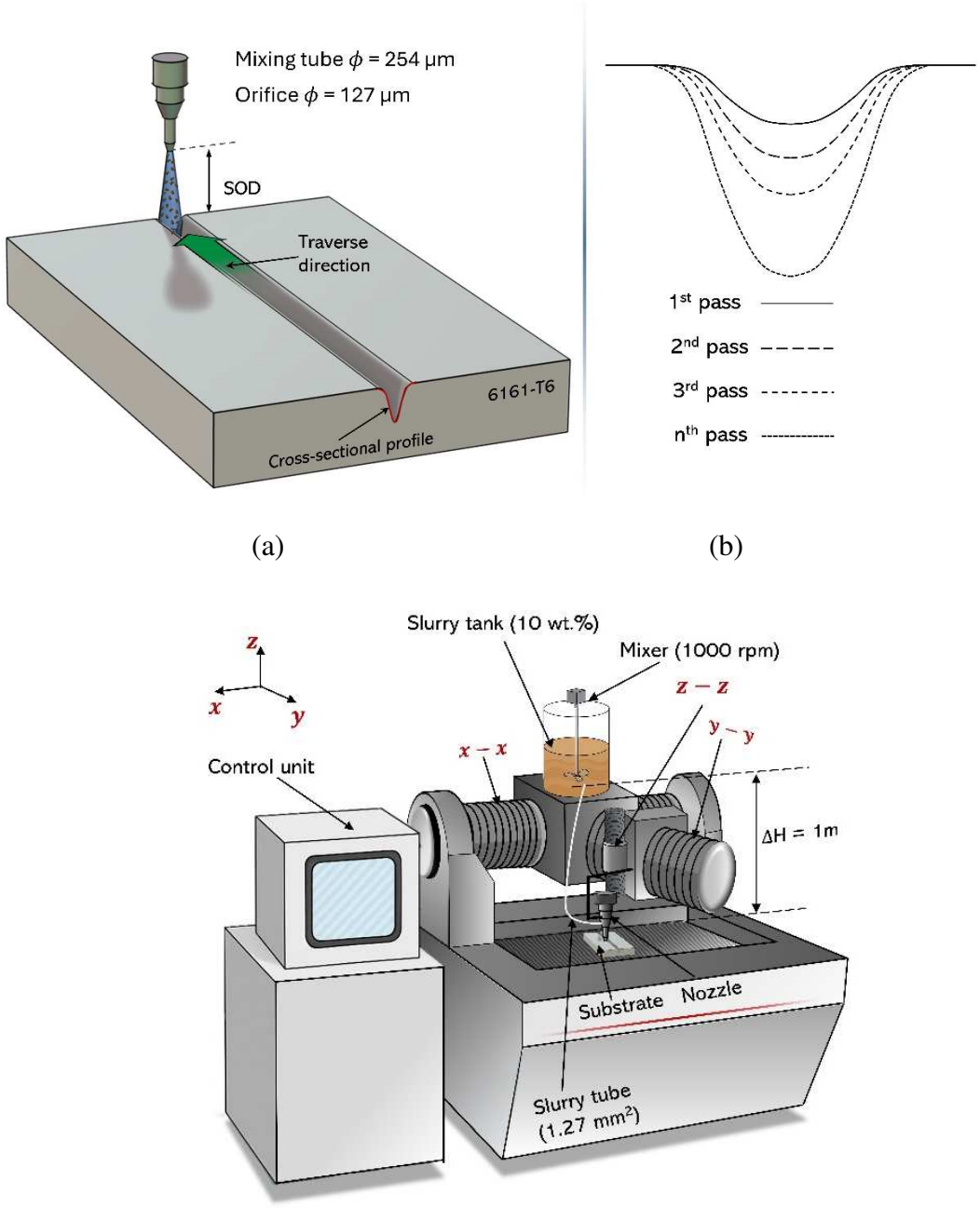


Fig. 1. Schematics of (a) a channel milled on 6061-T6 substrate. (b) Cross-sectional profiles of multi-pass channels. (c) The ASJM setup.

3. Predictive models

This section presents the supervised learning models developed to predict the cross-sectional surface profiles of the channels milled using ASJM. All models take as input the four key process parameters, i.e. *P*, *V*, *SOD*, and *N*. The target output is a 220-dimensional vector representing the depth coordinates along the channel cross-sectional profile.

Two categories of predictive models were considered. The first comprises traditional ML models, including polynomial regression and random forest regression. Because such approaches are interpretable and computationally efficient, they served as good baselines for assessing nonlinear relationships. The second group consists of deep neural networks, including a fully connected architecture (commonly referred to as an artificial neural network, ANN) and a one-dimensional convolutional neural network (1D-CNN). The former models nonlinear relationships directly between input parameters and surface profiles, while the latter leverages convolutional layers to capture local spatial correlations along the profile. The Python codes of all models are provided in the supplementary materials.

Each model was trained using 85% of the data, with the remaining 15% reserved as a hold-out test set. Model performance was evaluated using three standard regression metrics: mean squared error (MSE), mean absolute error (MAE), and the coefficient of determination (R^2). These metrics provide complementary perspectives on predictive accuracy. The MSE is defined as

$$MSE = \frac{1}{n}\sum_{i=1}^{n}(z_i - \hat{z}_i)^2, \tag{1}$$

where z_i and $\hat{z}_i$ denote the true and predicted values at point i, respectively, and n is the total number of predicted values in the profile. MSE penalizes larger errors more severely due to the squaring operation, making it particularly sensitive to outliers. The MAE is defined as

$$MAE = \frac{1}{n}\sum_{i=1}^{n}|z - \hat{z}_i|, \tag{2}$$

and provides an interpretable measure of the average absolute deviation between the predicted and actual values. Unlike MSE, MAE treats all errors linearly and is therefore more robust to large deviations in isolated points. Finally, R^2 measures the proportion of variance in the true output that is captured by the predictions. It is given by

$$R^2 = 1 - \frac{\frac{1}{n}\sum_{i=1}^{n}(z_i - \hat{z}_i)^2}{\frac{1}{n}\sum_{i=1}^{n}(z_i - \bar{z})^2}, \quad (3)$$

where $\bar{z}$ is the mean of the true values. An R^2 score of 1 indicates perfect predictions, while a value near 0 indicates that the model fails to explain the variability in the data.

3.1. Traditional Machine Learning Models

Traditional ML models offer interpretable baselines for predicting ASJM surface profiles. This section explores two such approaches: polynomial regression, which captures nonlinearities through feature expansion, and random forest regression, which models complex interactions using an ensemble of decision trees. Both are evaluated as reference points for comparison with deep learning models.

3.1.1. Polynomial Regression

Polynomial regression is employed as a parametric method to model the nonlinear interactions between the ASJM input variables. All regression analyses were implemented in Python using the *scikit-learn* library. Polynomial feature expansion and regression were performed with the Polynomial Features and Linear Regression modules of *scikit-learn*.

The original input space is expanded using polynomial feature transformation, where interaction terms and higher-order powers are systematically generated. This feature expansion enables the model to approximate complex, nonlinear mappings without explicitly defining interaction structures. All transformed features are standardized using z-score normalization before being passed to a multi-output linear regression model, allowing the model to treat all features on a comparable scale.

To determine the optimal model complexity, a range of polynomial degrees from 1 to 5 is evaluated using three-fold cross-validation on the training data. For each degree, the model is trained on two folds and validated on the third, with the process repeated to cover all fold combinations. Model performance is assessed using three metrics: MSE, MAE, and R^2. These metrics provide insight into the model's pointwise accuracy, average error magnitude, and ability to explain variance in the output profiles, respectively. The degree that yields the highest average R^2 across validation folds is selected as the optimal complexity, balancing model expressiveness with generalization. This final configuration is then retrained on the entire training set and evaluated on the test set to estimate its real-world predictive performance. The

resulting model serves as a baseline for comparing the performance of more flexible nonlinear models such as random forests and deep neural networks.

3.1.2. Random Forest Regression

Random forest regression is introduced as a non-parametric ensemble approach capable of modeling complex, nonlinear relationships among input variables without requiring prior assumptions about functional form. The random forest models were developed in Python using the scikit-learn library, employing the Random Forest Regressor class with hyperparameter tuning through grid search and cross-validation.

As depicted in Fig. 2, the method constructs an ensemble of decision trees, each trained on a random subset of the data and features, aggregating their predictions to improve generalization and reduce overfitting. In addition to the four raw ASJM input features, three additional engineered features are incorporated to encode domain-specific relationships. These include the product of pressure and number of passes (P×N), which, for a constant abrasive concentration, is indicative of the cumulative erosive potential delivered to the surface; the product of stand-off distance and traverse speed (SOD×V), capturing the dispersion and exposure characteristics of the jet; and the ratio of pressure to speed (P/V), assessing the erosive potential per unit length of jet traverse.

Hyperparameter optimization was performed using an exhaustive grid search with three-fold cross-validation. The hyperparameters considered include the number of trees in the ensemble (100, 200, 300), the maximum allowable depth of each tree (10, 15, 20, or unlimited), and parameters regulating node splitting: minimum samples required to split an internal node (2 or 5) and minimum samples required to be at a leaf node (1 or 2). Each candidate configuration is evaluated based on the average MSE across the validation folds. The configuration yielding the lowest validation MSE is selected as the optimal model.

Once the best configuration was identified, the model was retrained on the full training dataset and evaluated on the held-out test set using MSE, MAE, and R^2. This procedure ensured robust generalization and facilitated fair comparison with other modeling approaches. Due to its ensemble nature and feature subsampling, the random forest model is particularly well-suited for capturing feature interactions and mitigating the effects of noise in high-dimensional regression problems.

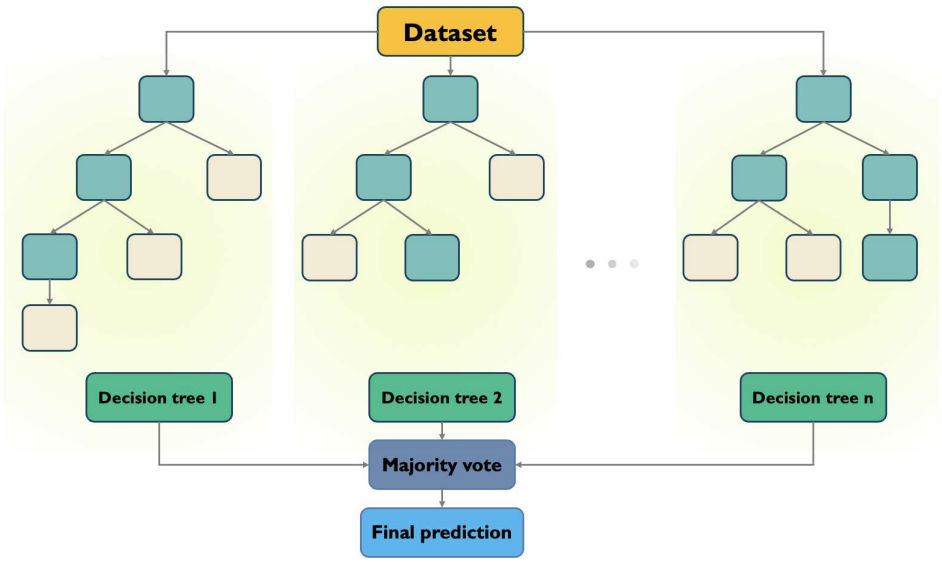


Fig. 2. Schematic representation of the structure of a typical random forest algorithm with three decision trees.

3.2. Deep Learning Models

Deep learning models are employed in this study to address the challenge of mapping ASJM process parameters to a high-dimensional vector of coordinates of the surface profiles, which are inherently nonlinear and structurally complex. These models are particularly suitable for this task because they are capable of learning rich, hierarchical representations directly from data, without the need for manual feature engineering or prior assumptions about the form of the relationships.

In the context of ASJM, each prediction corresponds to a full surface profile, a vector of depth values sampled across the channel width, which exhibits spatial continuity, smooth transitions, and localized geometric variations. These characteristics make deep learning architectures, especially neural networks, highly advantageous. Their capacity to model both global nonlinear dependencies and local spatial structures aligns naturally with the profile prediction task. Two deep neural network architectures were explored in this work: a fully connected deep neural network (commonly referred to as an ANN) and a 1D-CNN.

The ANN is designed to approximate complex, nonlinear mappings between the four input parameters and the full profile vector. The 1D-CNN, in contrast, incorporates convolutional layers to explicitly exploit the spatial organization of the output by learning translation-invariant filters that detect localized features along the profile. Both models are trained in a supervised manner using normalized input features and scaled outputs, and extensive hyperparameter tuning is conducted to ensure optimal performance. Model evaluation focused

on the accuracy of predicted profiles and the ability to generalize to unseen machining conditions.

3.2.1 Artificial Neural Network

The artificial neural network, implemented here as a fully connected deep neural network, consists of multiple hidden layers, each followed by a nonlinear activation function to enable the modeling of complex, non-linear relationships between input parameters and profile outputs. The ANN models were implemented in Python using *TensorFlow* and its *Keras* API. Model construction, training, and evaluation employed Sequential models with Dense, Dropout, and standard optimization callbacks such as Early Stopping. Both the input features and the output surface profiles were standardized using z-score normalization prior to training to ensure numerical stability and accelerate convergence.

A comprehensive hyperparameter search was conducted to identify the optimal network configuration. This search explored variations in the number of hidden layers (ranging from 1 to 3), the number of neurons per layer (32, 64, and 128), activation functions (ReLU and tanh), dropout rates (0.1, 0.2, and 0.3) for regularization, optimization algorithms (Adam and RMSprop), learning rates (1e-4, 1e-3, and 5e-3), and batch sizes (16, 32, and 64). These hyperparameter ranges follow standard practices commonly reported in the deep learning literature [28,29].

For each candidate configuration, the model was trained using early stopping based on validation loss, with a patience threshold of 50 epochs to prevent overfitting while allowing sufficient training flexibility. The best-performing configuration was identified based on the lowest validation MSE. This selected model was then retrained on the entire training dataset and evaluated on the hold-out test set. The predicted output profiles were inverse-transformed to recover their physical scale, enabling both quantitative evaluation through standard regression metrics and qualitative assessment via profile visualization. The ANN's ability to model complex nonlinearities makes it a strong candidate for full-profile prediction in ASJM, especially in capturing smooth transitions and subtle local variations.

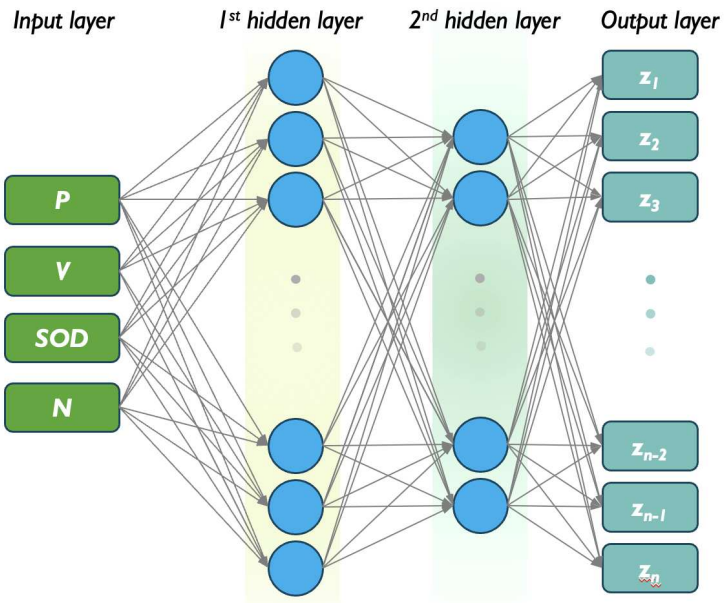


Fig. 3. Schematic representation of the structure of a typical ANN algorithm with four inputs and two hidden layers.

3.2.2 Convolutional Neural Network

To further exploit the spatial continuity and local structure inherent in the machined surface profiles, a one-dimensional convolutional neural network (1D-CNN) was implemented. Unlike the fully connected ANN, the CNN architecture leverages convolutional filters to extract localized features along the output vector, making it particularly well-suited for capturing depth variations and curvature across spatial positions. The CNN models were implemented using *TensorFlow* with the *Keras* deep learning API in Python. The architecture included 1D convolutional, dropout, flattening, and dense layers, trained with the Adam and RMSprop optimizers under early stopping criteria.

The four standardized Input features are reshaped into a format compatible with 1D convolution, where each feature vector is treated as a single-channel sequence input.

The architecture comprises a single convolutional layer, followed by dropout regularization to mitigate overfitting. This is followed by a flattening operation and a fully connected layer that maps the extracted features to the final predicted surface profile. A focused hyperparameter search was conducted to identify the optimal configuration. The search explored combinations of the number of filters (16 and 32), kernel sizes (1 and 2), dropout rates (0.1 and 0.2), and optimizer types (Adam and RMSprop). Each candidate model was trained using early stopping based on validation loss, with a patience threshold of 50 epochs, consistent with the procedure adopted for the ANN. The configuration achieving the lowest validation

mean squared error was selected as the final model. Predictions from this model were inverse-transformed to the original scale and evaluated on the test set using standard regression metrics. Visual comparison with ground truth profiles demonstrated the CNN's capability to accurately reproduce complex surface geometries, especially in regions exhibiting smooth transitions and localized features. The use of convolution thus provided a structurally informed alternative to fully connected architectures in modeling spatially correlated outputs.

4. Results and discussion

This section presents a comprehensive evaluation of the predictive models developed in this study. The analysis highlights the relative strengths of traditional ML and deep learning approaches, with special attention to their ability to capture machined channel depth, width, and overall topography. Representative and worst-case predictions were used to illustrate model reliability across a wide range of machining conditions. In addition to performance comparison, further investigations were conducted to assess the models' sensitivity to the size and resolution of the training data. These experiments help evaluate model robustness and data efficiency. Furthermore, the inverse capability of the models to predict the process parameters needed to machine the desired topographies was studied.

4.1. Prediction results

This section presents the predictive performance of the four developed models trained to estimate surface profiles from ASJM input parameters. Each model was trained on 85% of the dataset and evaluated on the remaining 15% test set. The performance was reported using MSE, MAE, and R^2, capturing both local accuracy and global profile consistency. Four representative test samples that span a wide range of aspect ratios were selected to visualize the performance.

The Polynomial Regression model serves as a parametric baseline and was tuned by cross-validating polynomial degrees from 1 to 5. It was concluded that third degree yielded the best tradeoff between complexity and generalization, achieving an MSE of 0.000086 mm2, MAE of 0.00441 mm, and R^2 of 0.7728 on the test set. As shown in Figure 4, the model captured the general shape of cross-sectional profiles as well as their depth and width over a wide range of aspect ratios with reasonable accuracy. As a context for the reported errors, the experimental scatter in depth of micro-channels milled with ASJM is typically reported to be between 5% to 15% of the channel's depth [12,30].

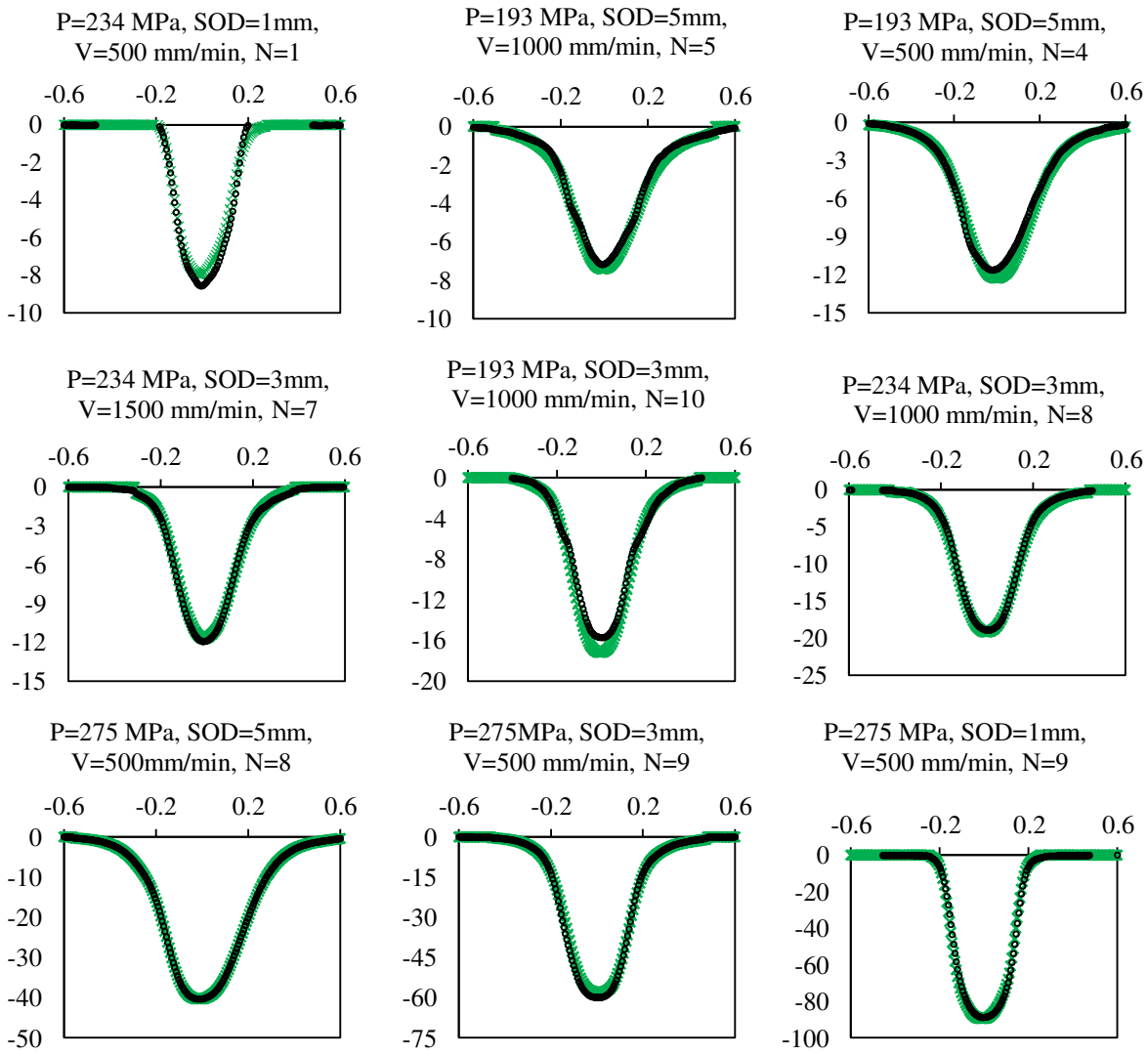


Fig. 4. Predicted (•) vs. measured (×) surface profiles using the Polynomial Regression model (degree = 3) for 9 different sets of operating parameters. In all graphs, horizontal axis is width [mm], and the vertical axis is depth [10^{-2} × mm].

The Random Forest model, a non-parametric ensemble learner, was trained with a grid search over depth, number of trees, and node-splitting criteria. The best configuration included 300 trees with a maximum depth of 20 and default node constraints. This model achieved MSE = 0.000127 mm^2, MAE = 0.00453 mm, and R^2 = 0.7582 on the test set. While slightly less accurate than the polynomial model in terms of R^2, the random forest demonstrated improved performance on diverse profiles, especially when enhanced by domain-informed feature engineering (P×N, SOD×V, and P/V). Figure 5 illustrates that the RF model performed robustly across various profiles and benefitted from the additional engineered features.

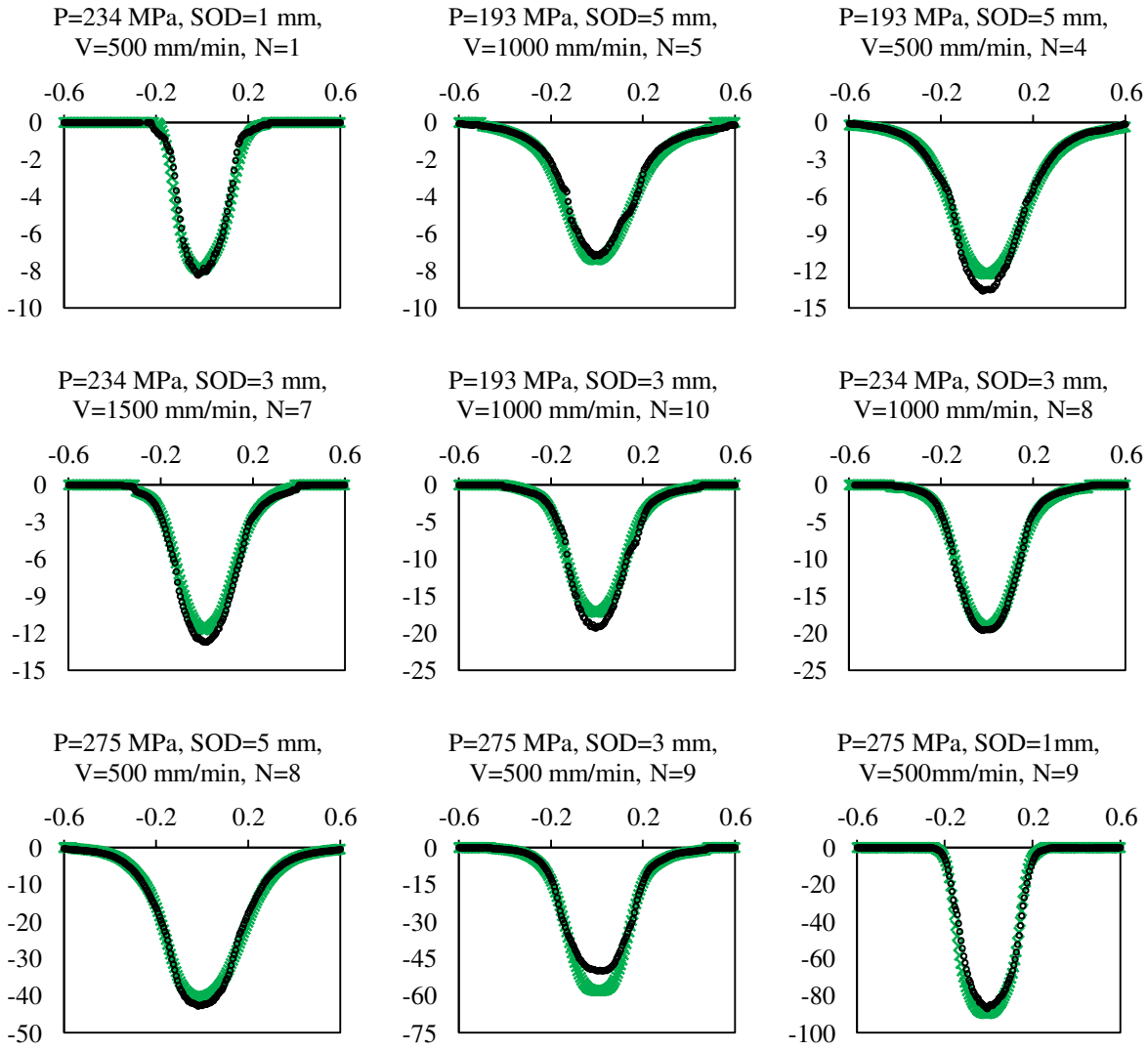


Fig. 5. Predicted (•) vs. measured (×) surface profiles using the Random Forest model for 9 different sets of operating parameters. In all graphs, horizontal axis is width [mm], and the vertical axis is depth [10-2 × mm]. The model performs robustly across diverse aspect ratios, benefiting from engineered features to improve expressiveness.

The Artificial Neural Network yielded the strongest test performance among all models, achieving the lowest MSE (0.000048 mm^2) and MAE (0.00339 mm), and the highest R^2 (0.8170). The best architecture featured two hidden layers with 64 neurons, a dropout rate of 0.3, and RMSprop optimizer with a learning rate of 0.005. This model demonstrated a strong ability to generalize and accurately replicate profile curvature, sidewall asymmetry, and depth, as illustrated in Figure 6. The ANN captured both depth and sidewall variation across all the profiles, including subtle curvatures. Its flexibility allowed it to handle complex shapes while maintaining smooth and realistic output.

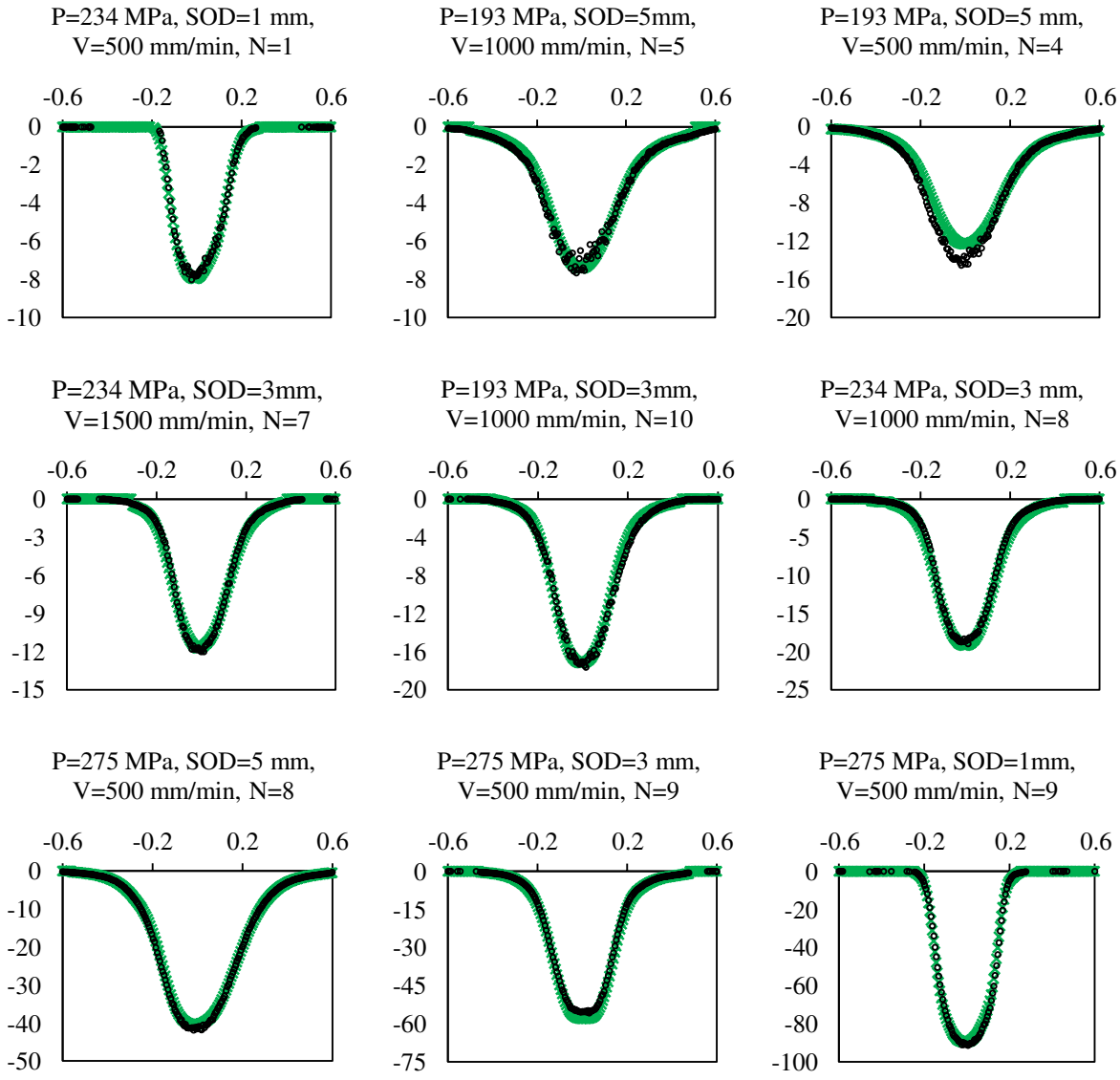


Fig. 6. Predicted (•) vs. measured (×) surface profiles using the ANN model for 9 different sets of operating parameters. In all graphs, horizontal axis is width [mm], and the vertical axis is depth [$10^{-2} \times$ mm].

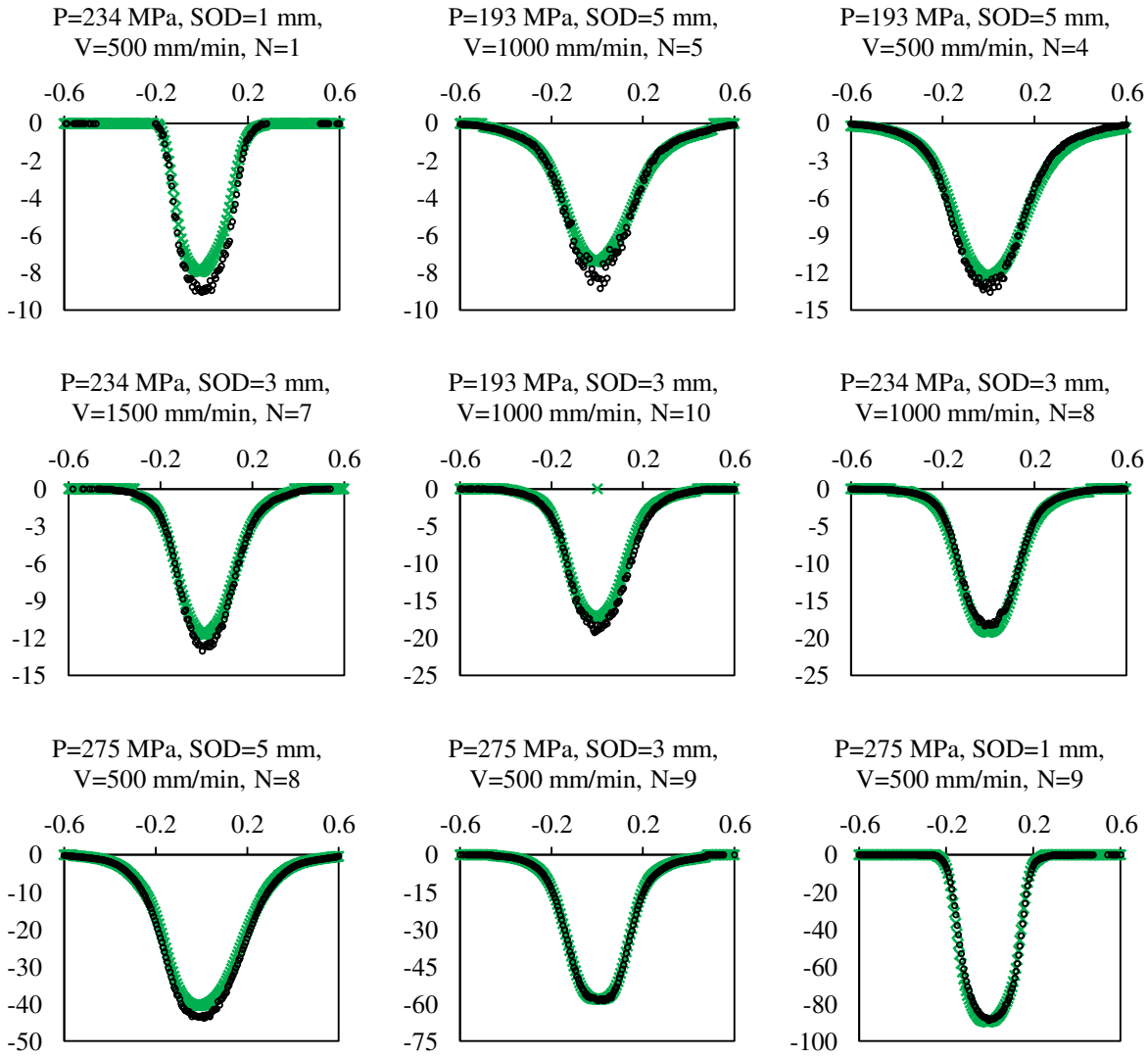


Fig. 7. Predicted (•) vs. measured (×) surface profiles using the CNN model for 9 different sets of operating parameters. In all graphs, horizontal axis is width [mm], and the vertical axis is depth [10^{-2} × mm].

The optimal configuration for the Convolutional Neural Network included 32 filters, kernel size 1, and dropout 0.1 that achieved MSE = 0.000068 mm^2, MAE = 0.00427 mm, and R^2 = 0.8070. While slightly behind ANN in global metrics, the CNN performed competitively and consistently reconstructed the smooth contours and symmetrical features, as shown in Figure 7. Some distortion appeared in narrow or steep profiles, where localized filters may be insufficiently expressive.

The quantitative results plotted in Fig. 8 highlight clear differences in predictive performance among the four modeling approaches. The artificial neural network achieves the

highest overall accuracy, with the lowest mean squared error (0.000048) and mean absolute error (0.00339), as well as the highest coefficient of determination ($R^2 = 0.8170$), indicating a superior ability to capture both the global variance and the local profile details. The convolutional neural network also performed strongly, achieving the second-highest R^2 (0.8070) and outperforming the regression-based models in terms of MSE. Polynomial regression and random forest models delivered reasonable performance, with R^2 values of 0.7728 and 0.7582, respectively. While random forest benefits from feature engineering and non-parametric flexibility, it is ultimately outperformed by the more expressive neural network architectures. Overall, the table implies that deep learning models, particularly the ANN, are best suited for high-fidelity prediction of ASJM surface profiles, offering a clear improvement over traditional machine learning models.

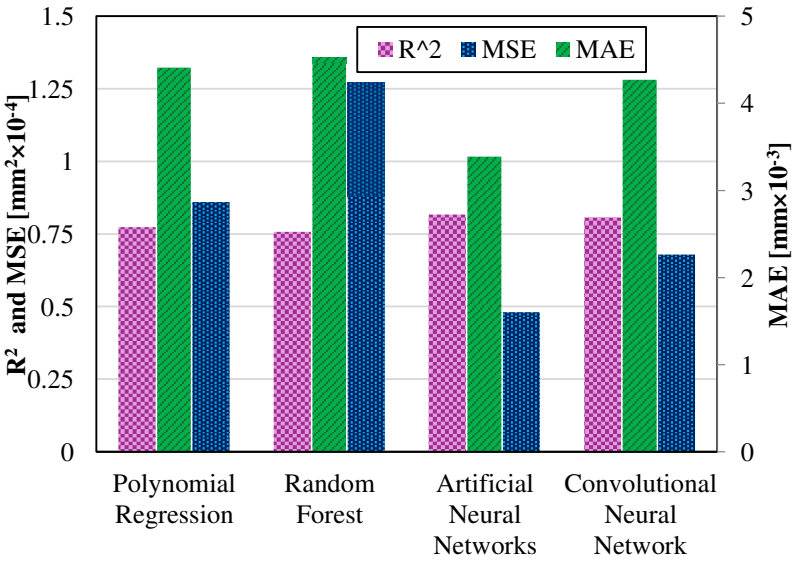


Fig. 8. Quantitative comparison of model performance on the test set using MSE, MAE, and R^2 for polynomial regression, random forrest, ANN, and CNN models

4.1 Aspect-ratio analysis, latency, and noise robustness

The test folds were split by channel aspect ratio (for $AR < 0.5$, $0.5 \leq AR < 1.5$, and $AR \geq 1.5$, $n = 28$, 7, and 6 channels, respectively) to see where the differences between models actually appear. For shallow channels, all four models gave a similar MAE, between 2.5 and 5.6 µm. The differences appeared on the deepest channels, where the CNN kept its accuracy at 4.5 µm, while the polynomial baseline rose to 7.6 µm and the random forest degraded sharply to 15.2 µm. Therefore, a CNN-based forward model is preferred when high-aspect-ratio features are desired, for example biomedical micro-fluidic channels and MEMS cavities, where geometric tolerance is the priority (see Fig 9).

Per-sample inference time on a single CPU varies by four orders of magnitude between the candidate models. As shown in Fig. 10a, polynomial regression, ANN, CNN, and random forest models typically take 0.22 ms, 117 ms, 106 ms, 10.9 s per sample to complete, respectively. The much higher computational cost of the random forest comes from predicting all 220 points of the profile vector with 300 deep trees. Thus, despite its accuracy, this rules it out as the back-end of a real-time controller. The two deep networks are well below the millisecond-per-pass budget that production traverse speeds would require for closed-loop correction.

To test the sensitivity to measurement noise on the four process inputs, zero-mean Gaussian perturbations of standard deviation σ = 1, 2, 5 and 10 % of each feature's empirical spread at inference time were added and the held-out folds (Fig. 10b) were re-evaluated. The MAE of both deep models rose only mildly, from 3.5 µm at σ = 0 to about 4.1 µm at σ = 10 %, and that of the random forest from 5.5 to 6.0 µm. The trained surrogates therefore tolerate realistic sensor noise on the four process inputs. The degree-3 polynomial baseline however behaved differently: as soon as noise was added, the cubic cross-terms amplified perturbations in the standardised feature space and the predictions diverged to non-physical values. The polynomial trace from Fig. 10b was omitted for clarity. This is itself an argument against using high-degree polynomial surrogates in a production setting where some amount of measurement noise is unavoidable.

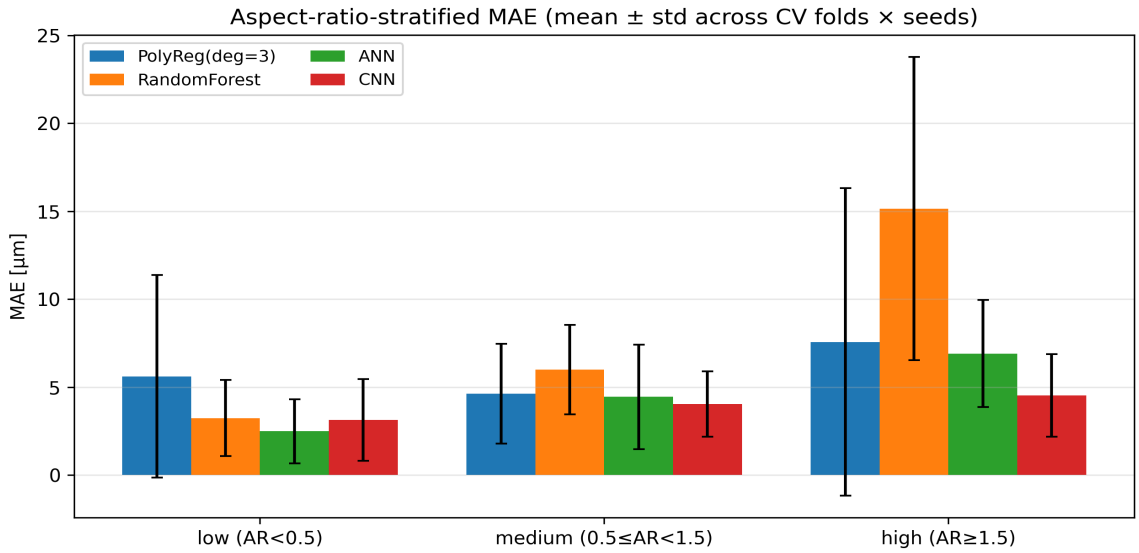


Fig. 9. Aspect-ratio-stratified MAE on the held-out folds, separating low/medium/high-AR channels.

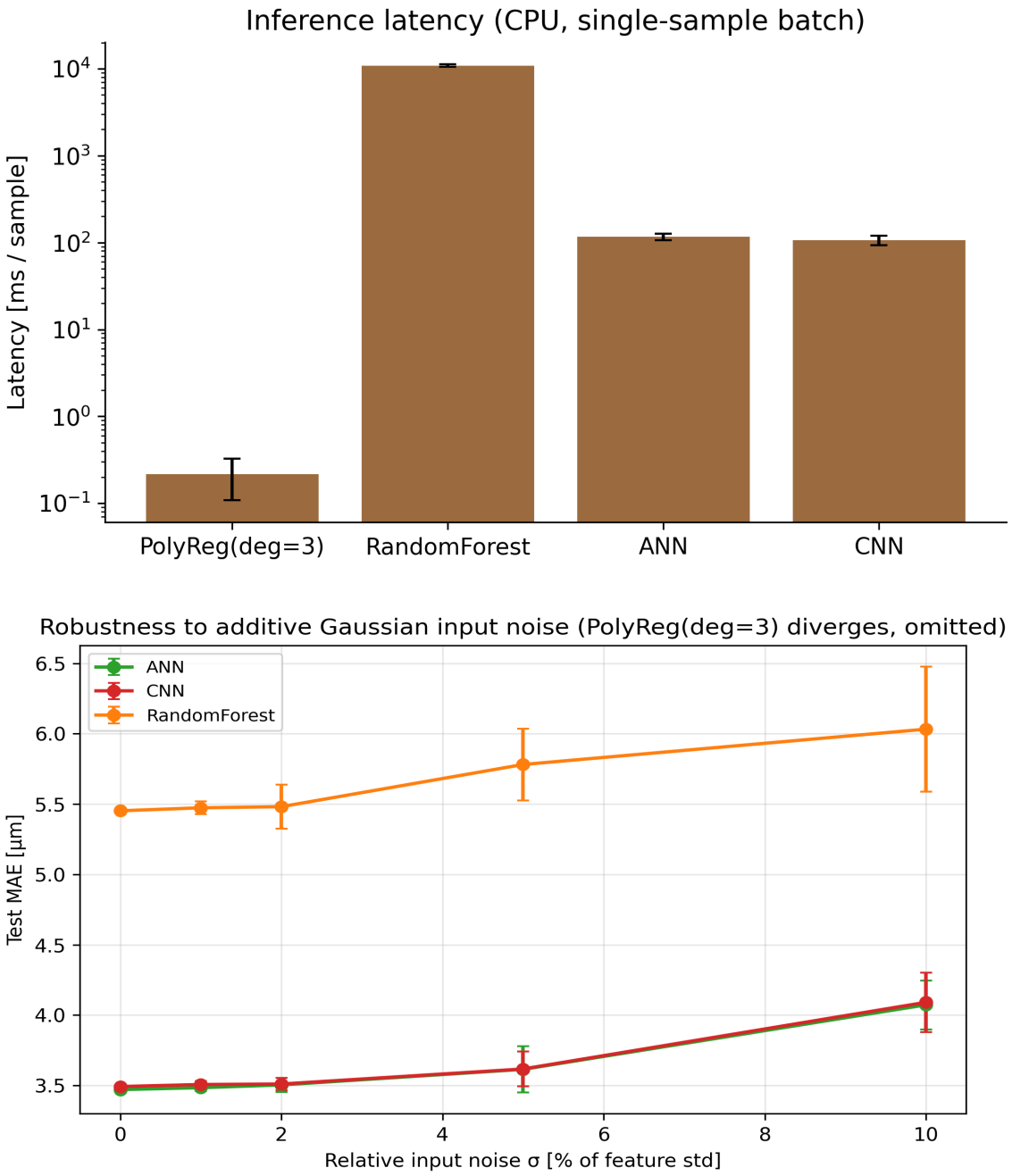


Fig. 10. (a) Per-sample CPU inference latency and (b) MAE versus standard deviation of additive Gaussian noise on the input parameters.

4.2. Sensitivity of outputs to database size

To evaluate the robustness and data efficiency of the predictive models, a systematic investigation was conducted to assess the impact of dataset size on model performance. Four different dataset sizes including 25%, 50%, 75%, and 100% of the full dataset were selected to simulate varying levels of data availability. For each subset, samples were selected in a uniformly distributed manner across the full design space to maintain representativeness and

coverage. A fixed test set was held constant across all scenarios to ensure fair and consistent evaluation. Importantly, model selection and hyperparameter tuning were performed independently for each dataset size. This ensured that performance metrics reflected what is realistically achievable under data-limited conditions, without relying on configurations optimized for the full dataset. This approach enabled an accurate assessment of how model accuracy scales with data availability, offering insight into the minimum data requirements for reliable surface profile prediction in ASJM and whether performance gains plateau beyond a certain dataset size.

Line graphs of Fig. 11a-c compare the MSE, MAE, and R^2, respectively for all the utilized machine learning models when trained with 25%, 50%, 75%, and 100% of the experimental dataset. The Random Forest model's performance was significantly worse when using only 25% of the dataset, leading to MSE, MAE, and R^2 values of 0.00188 mm^2, 0.0138 mm, and 0.32 respectively. For other models, although their performance experienced a meaningful drop at a 25% dataset size, they could still achieve reasonable accuracy with R^2 of above 0.6 and MSE and MEA of below 0.008 mm^2 and 0.01. The most accurate results using a 25% dataset size were obtained using ANN with R^2 value of 0.7, implying that it was capable of reproducing the results with high robustness even with small dataset sizes, making it the most efficient in terms of data collection. In all models, the R^2 value began to plateau after 75% of the dataset was used, with an average increase of ~3.2% after this point.

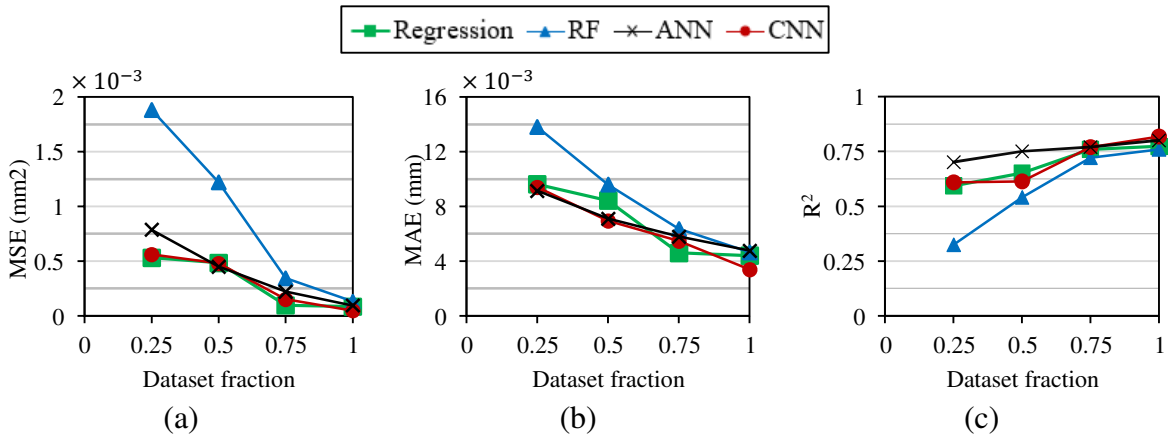


Fig. 11. Comparison of the performance of Polynomial Regression, RF, ANN, and CNN to dataset size in terms of (a) MSE, (b) MAE, (c) R^2 when using 25%, 50%, 75% and 100% of the experimental dataset.

4.3. Inverse modeling

In addition to the forward problem that predicts surface profiles from known process parameters, the developed machine learning models can also be applied in reverse to estimate the machining parameters required to achieve a specified channel topography. This approach is valuable for process planning and control in cases where a particular desired surface geometry is known in advance. In this study, an initial inverse modeling framework was designed that uses cross-sectional topographical features (i.e., depth and width) as inputs and determines a feasible set of process parameters (P, SOD, V, and N) required to machine the topography. The measured channel depths and widths of all the machined channels were paired with the corresponding process parameters. The dataset was split into training and validation subsets to ensure robust evaluation. Later, the full surface profile (as opposed to only the depth and width) was used as the input.

The inverse ANN took depth and width as inputs and determined continuous values of P, SOD, and V, together with a categorical probability distribution for N. However, because multiple parameter combinations can lead to the same geometry (many-to-one mapping), supervised loss with respect to the original parameters was not relied on solely. Instead, the predicted parameters were passed through the pre-trained forward ANN during training, which generated a simulated profile. The forward model's accuracy was verified in Section 4.1, and thus it was assumed that it could be used to validate the reverse model's predictions. Depth and width were then extracted from this simulated profile and compared to the target geometry. This "forward-consistency" loss ensured that the inverse ANN produced parameters which actually reproduced the desired geometry, rather than simply approximating the training labels.

Model performance was therefore evaluated primarily in terms of how well the reconstructed profiles matched the target depth and width. Errors were reported MAE, MSE, and R^2 for depth and width obtained from the forward check. Once trained, the inverse ANN can recommend a single feasible set of process parameters for any new target geometry, which can then be verified using the forward model if desired. Figure 12 shows the inverse designed modeling workflow.

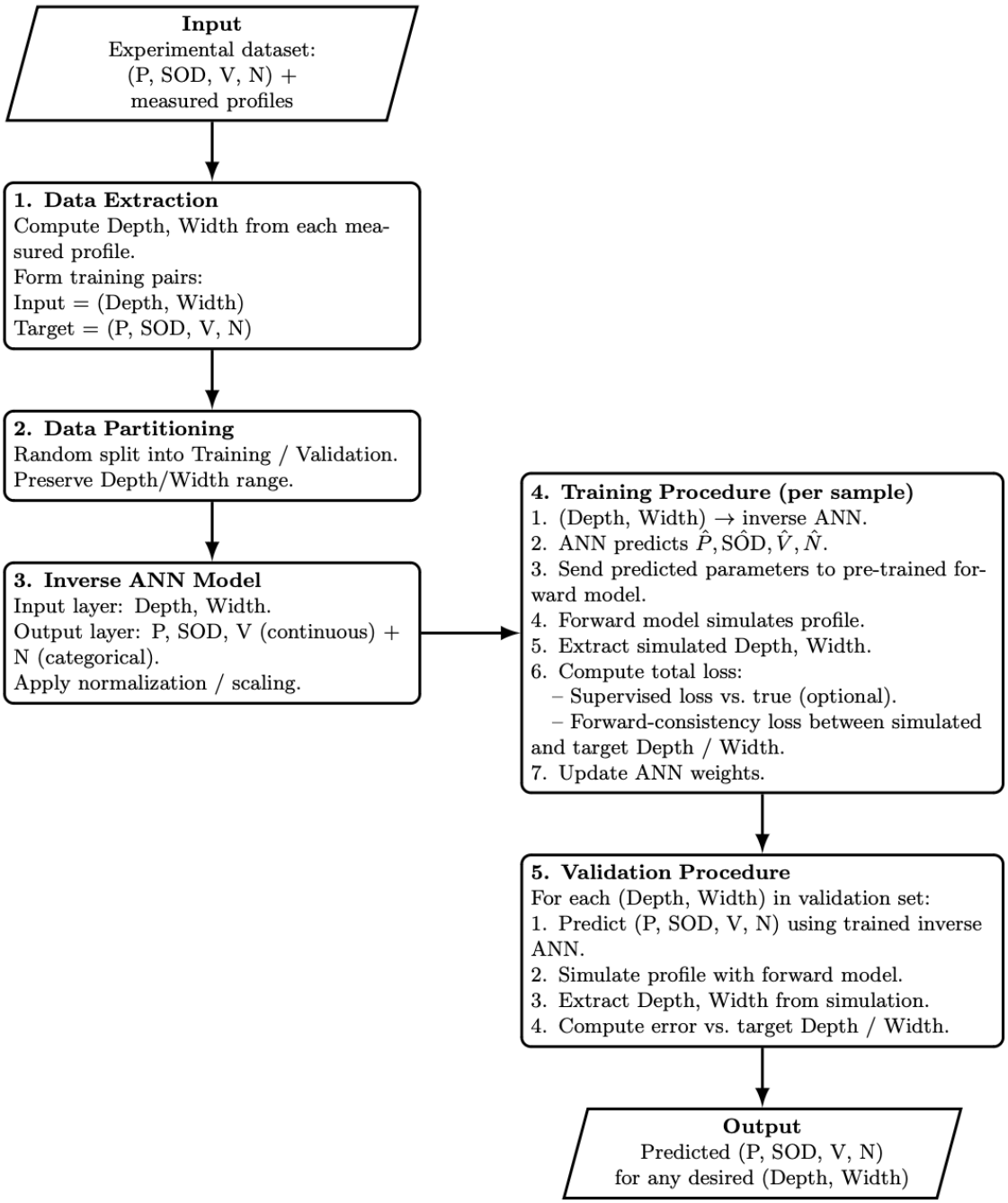


Fig. 12. Inverse modeling workflow. The inverse ANN maps target Depth and Width to process parameters (P, SOD, V, N). A pre-trained forward model enforces physical consistency by comparing simulated and target Depth/Width.

The inverse ANN was trained using the forward-consistency approach to predict one feasible set of process parameters from any specified channel cross-sectional topography, characterized by its depth and width. Because of the many-to-one mapping, the evaluation emphasized how accurately the predicted parameters could reproduce the target geometry rather than matching the original process settings exactly. After training, when the predicted parameters were passed through the previously trained forward ANN to reconstruct the

machined profile, the resulting depth showed good agreement with the targeted values, while the width showed moderate agreement. Specifically, for the depth, the model achieved an MAE of approximately 0.034 mm, an MSE of approximately 0.002 mm2, and an R^2 of 0.94. For width, an MAE of approximately 0.018 mm, an MSE of approximately 0.00067 mm2, and an R^2 of 0.55 were achieved. These results demonstrate that the inverse model can successfully generate process parameters that produce machined geometries closely matching the desired dimensions. Practically, this means the framework can recommend one feasible set of operating conditions that reproduces the target machined shape, providing a direct pathway from specified geometry to process settings and enabling profile-level process planning and control.

Figure 13 illustrates 9 representative case studies comparing the true and reconstructed cross-sectional profiles obtained by the proposed inverse modeling framework. Here, *true* refers to the desired profile obtained experimentally and used as input to the inverse model, while *reconstructed* denotes the profile generated by the forward model using the operating parameters predicted by the inverse model. The true profiles are in good agreement with the forward model's predictions, accurately capturing both the overall machined shape and the maximum depth. Even with variations in process parameters, the reconstructed geometries remain highly consistent with the targets. These examples highlight the ability of the inverse model not only to recommend feasible process settings but also to ensure that the resulting profiles match the desired dimensions.

In more precise or high-value applications, achieving a specific channel shape is necessary, as opposed to just meeting the depth and width targets [31]. To infer feasible process parameters for a desired full topography, an inverse ANN was developed that takes the entire measured surface profile as input rather than only depth and width. Because the number of profile points (~220 per sample) was large relative to the dataset size (N=270), the profile was first downsampled by taking every other point (~110 inputs) to reduce redundancy and stabilize learning while preserving the overall shape. The inverse ANN outputs continuous estimates of P, SOD, and V, together with a categorical distribution for N. During training, these predicted parameters are passed through the frozen forward ANN to reconstruct a full-resolution profile. The inverse loss combines (i) light supervision on the parameter heads (for stability) with (ii) a forward-consistency loss that penalizes the mismatch between the reconstructed and measured profiles (point-wise), optionally normalized by the profile standard deviation. This coupling ensures that the predicted parameters are physically consistent, i.e., they generate a realistic profile when evaluated by the forward model.

Similar to the first case, because of the many-to-one mapping, inverse quality was not evaluated by parameter error. Instead, the model was assessed strictly in the topography space: after the inverse ANN predicts parameters, the forward ANN reconstructs the profile, and MAE, MSE, and R^2 between reconstructed and predicted full profiles across the test set are reported. With this setup, the inverse model achieves low profile error (e.g., MAE $\approx$ 0.015 mm, MSE $\approx$ 0.002 mm^2) and strong agreement ($R^2 \approx 0.77$) while producing visually overlapping curves in representative case studies.

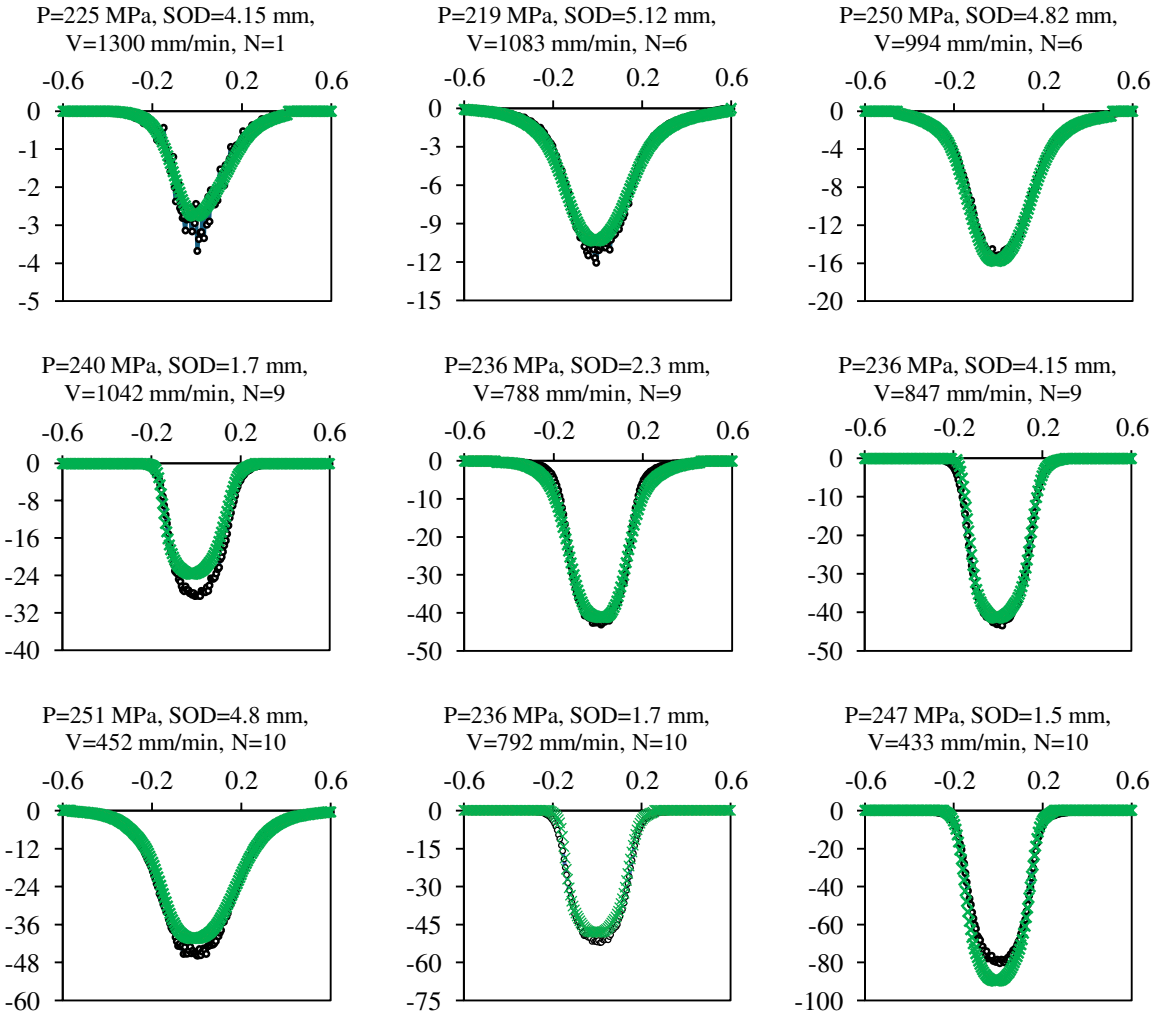


Fig. 13. reconstructed (•) vs. true (×) surface profiles using the ANN with desired width and depth inputs only for 9 different sets of operating parameters. In all graphs, horizontal axis is width [mm], and the vertical axis is depth [$10^{-2}\times$ mm]. Each graph shows a test sample with its predicted process parameters. Legends show the operating parameters predicted by the inverse model.

Figure 14 illustrates representative case studies comparing the true and reconstructed cross-sectional profiles obtained using the proposed inverse modeling framework for the case when the full desired profiles were used as inputs. As seen, when the full desired channel profiles were used as inputs for inverse modeling, the predictive accuracy declined compared to the case where only depth and width were provided. This is due to the increased input dimensionality and redundancy among profile points, which complicate the learning process and make the model more prone to overfitting and noise sensitivity. Channel profiles often contain highly correlated and noisy information that does not necessarily contribute additional predictive value, whereas using key geometric descriptors such as depth and width provides a more compact and physically meaningful representation of channel geometry.

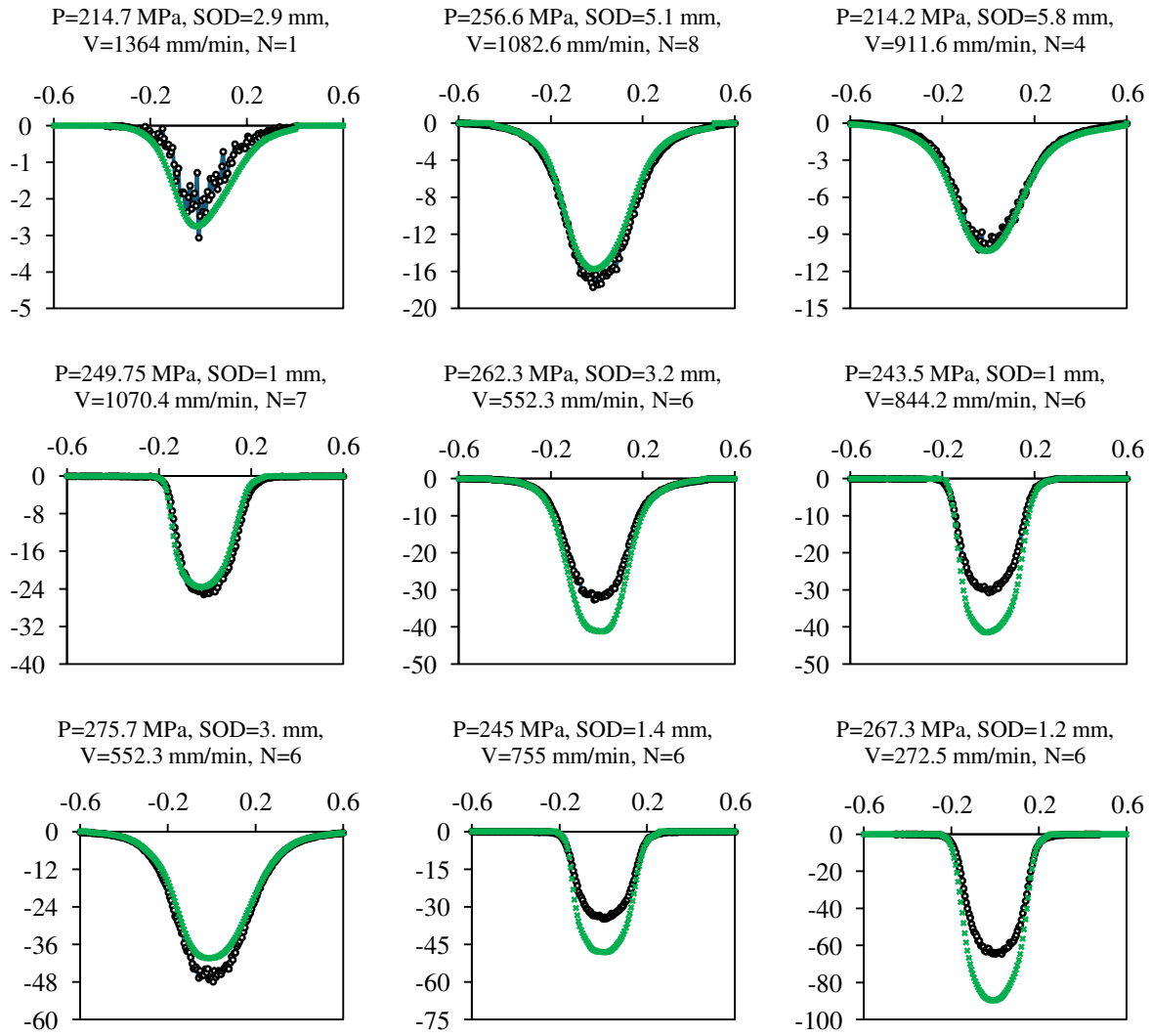


Fig. 14. reconstructed (•) vs. true (×) surface profiles using the ANN with full desired profile as input for 9 different sets of operating parameters. In all graphs, horizontal axis is width [mm], and the vertical axis is depth [10^{-2} × mm]. Each graph shows a test sample with its predicted process parameters. Legends show the operating parameters predicted by the inverse model.

4.3.1 Probabilistic inverse with constraint projection

Reporting a single feasible parameter set hides the fact that the inverse problem is many-to-one. To make the ambiguity explicit, a probabilistic inverse network was added that draws K = 50 stochastic samples per target by Monte-Carlo dropout and then projects each candidate onto the operating envelope ($P \in [193, 275]$ MPa, $SOD \in [1, 5]$ mm, $V \in [500, 1500]$ mm/min, integer $N \in [1, 10]$). On the held-out targets the best of the K candidates achieved a median absolute depth error of 0.94 µm and width error of 6.0 µm, with $R^2 = 0.985$ and MAE = 4.8 µm on the forward-reconstructed profile. These numbers are comparable to the forward model's own accuracy, which suggests that the inverse network is using essentially all the information in the geometric target. Figure 15 shows the Best-of-K reconstructed profiles versus desired targets for the probabilistic inverse network. The median of the K candidates is deliberately less accurate (depth MAE = 34.6 µm) because it averages across the multi-modal solution set; it is reported as a conservative operating point. The empirical spread of the K candidates, $\sigma(P) \approx 5.4$ MPa, $\sigma(SOD) \approx 0.32$ mm, $\sigma(V) \approx 55$ mm/min and $\sigma(N) \approx 0.45$ passes, expresses the many-to-one ambiguity in units that the operator can read directly. When the spread is small, the recommendation is effectively unique and when it is large, several physically distinct recipes can hit the same target, and the operator can choose the recipe that best suits secondary objectives such as cycle time or abrasive consumption. Fig. 16 shows the Per-parameter empirical uncertainty across the K candidates per target, expressed in machinist-facing units.

To make the practical implications more concrete, consider a job-shop operator who needs to machine a 0.40 mm deep, 0.30 mm wide micro-channel into AA6061-T6 on a slurry jet system. Using the framework, the operator queries the trained inverse network with the desired (depth, width) target. Within about 200 ms, the network returns K = 50 candidate parameter sets together with their empirical spread. All of these candidates are guaranteed to lie inside the ranges ($P \in [193, 275]$ MPa, $SOD \in [1, 5]$ mm, $V \in [500, 1500]$ mm/min, integer $N \in [1, 10]$). The forward CNN is then used to verify the predicted profile for the chosen candidate, giving the operator some closed-loop confidence before the first cut.

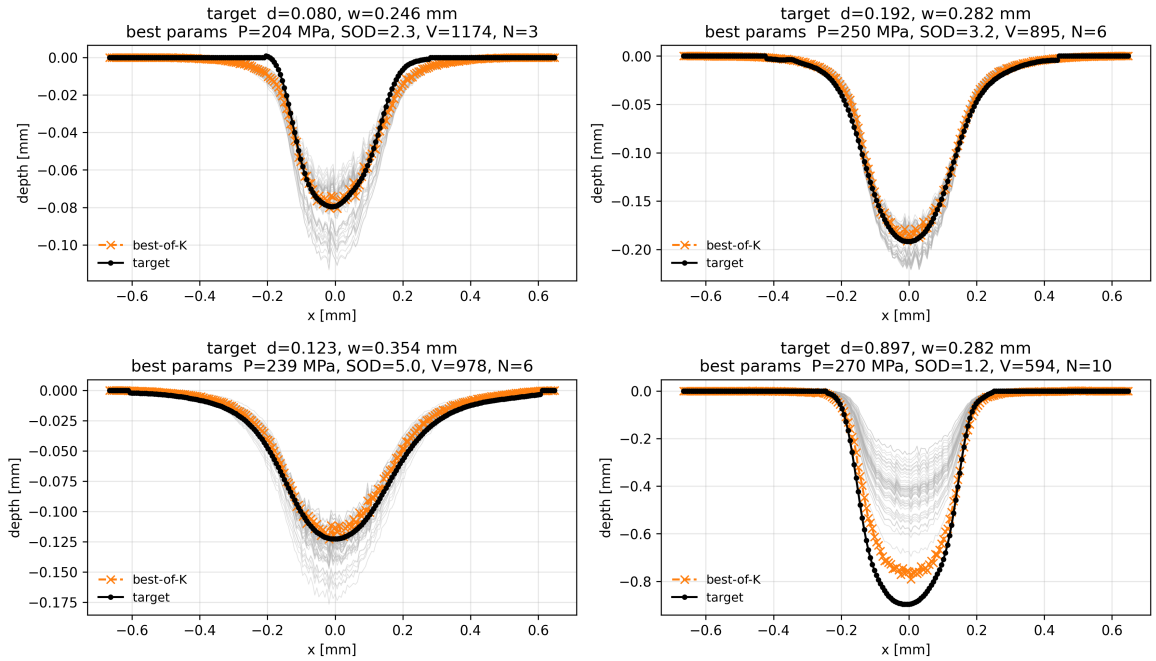


Fig. 15. Best-of-K reconstructed profiles versus desired targets for the probabilistic inverse network (K = 50 MC-dropout candidates per target).

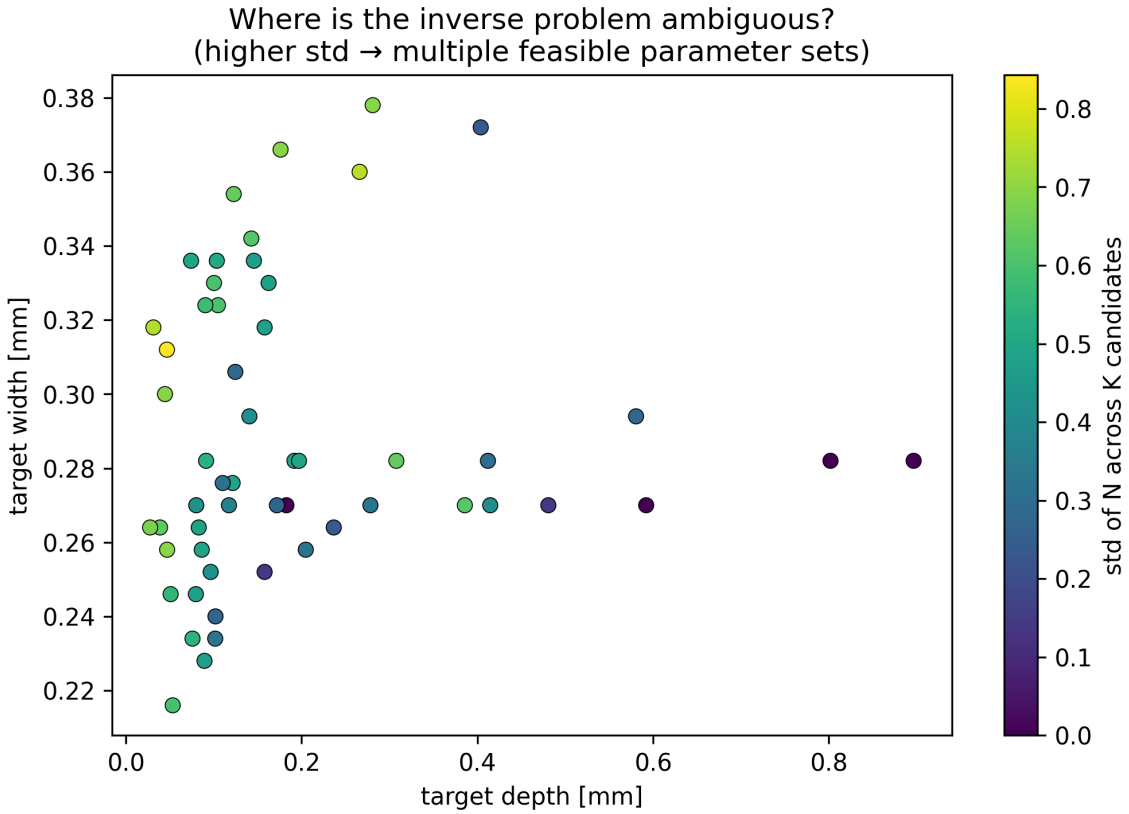


Fig. 16. Per-parameter empirical uncertainty across the K candidates per target, expressed in machinist-facing units.

4.4. Anticipated significance

Despite its compelling advantages, the principal industrial barrier to wider adoption of abrasive slurry jet micro-machining is the absence of fast, accurate predictive models that can be embedded in process planning and closed-loop control. The state-of-the-art surface-evolution simulations require hours of compute time per channel and cannot be inverted to recover the operating parameters needed for a desired geometry, while purely empirical look-up procedures require costly trial-and-error machining for every new material/geometry combination. The forward and inverse machine-learning surrogates introduced here address both shortcomings simultaneously: the forward models reduce per-prediction cost from hours to microseconds (a speed-up of approximately nine orders of magnitude relative to high-fidelity numerical simulation), while the constraint-aware inverse model enables one-shot specification of process parameters from a target geometry rather than an iterative search. In this regard, AI-powered manufacturing techniques could be integrated into the process, especially to serve as real-time digital twins. Nevertheless, prior to designing such systems, it is important to identify the capabilities and weaknesses of such statistical techniques. The presented work is a pioneering effort to investigate the feasibility of the use of ML to predict the nonlinear and complex material removal patterns in ASJM-based processes and how well these models respond to experimental datasets. A good example of future work is to train ML models to predict complex AWJ machined free-form surfaces. Furthermore, ML could be used to establish a relationship between the parameters that are measurable during the process (e.g., noise or vibration frequency). This way, by creating a closed loop between the pre-trained model and the process, real-time process monitoring and control could be achieved.

5. Limitations and validity envelope

The findings reported here apply within the experimental envelope used to generate the data. The dataset covers abrasive slurry jet micromachining at pump pressures of 193 to 275 MPa, stand-off distances of 1 to 5 mm, traverse speeds of 500 to 1500 mm/min, and 1 to 10 passes on AA6061-T6 with a garnet abrasive of nominal 33.6 µm diameter. Predictions outside this envelope, on different target materials, or with different abrasive types and sizes are extrapolations that have not been validated. The forward models show larger errors at the highest aspect ratios (AR > 1.5), where the steep sidewalls intensify secondary erosion mechanisms that are represented poorly in a training set of n = 270 samples. The inverse model returns a distribution of feasible solutions but does not guarantee global optimality and does

not account for random and systematic errors such as workpiece fixturing variability. All the models are tabular surrogates of stationary process conditions; they do not model transient phenomena such as start-of-pass acceleration or end-of-pass deceleration of the nozzle. These points define obvious directions for future work, including transfer learning to additional materials, and coupling the surrogate to an online optimiser that respects the constraints.

6. Conclusions

The present work investigated the feasibility of employing ML techniques to predict the surface topography of micro-channels machined using ASJM. Pump pressure, feed rate, SOD, and number of passes were selected as the operating parameters, each varied systematically according to a full factorial design of experiments. A total of 270 micro-channels were machined on AA6061-T6 substrates, with aspect ratios ranging from approximately 0.06 to 2. Four ML approaches were examined, including traditional models such as Nonlinear Regression and Random Forest, and deep learning models such as ANN and CNN. In addition, the ANN model was employed to address the inverse problem in predicting the operating parameters required to achieve targeted topographies. Overall, irrespective of channel aspect ratio, the ML models effectively captured the nonlinear dependencies of the ASJM process while providing predictive capability at a fraction of the computational cost of conventional numerical simulation methods. The combined forward and inverse modeling framework demonstrated a pathway toward automated control and optimization of ASJM processes, bridging the gap between empirical testing and real-time predictive manufacturing. Because the trained surrogates return predictions in about 100 ms on a typical desktop CPU, they remove the main computational obstacle that has so far prevented physics-based ASJM models from being placed inside a closed-loop controller, and they make in-process geometry correction, digital-twin process planning, and rapid qualification of new abrasive-target combinations practical without exhaustive design-of-experiments campaigns. The key conclusions are summarized as follows.

- All four models demonstrated strong predictive capability for the machined topographies, with MSE, MAE, and R^2 values ranging from 4.8×10^{-5} mm² to 1.27×10^{-4} mm², 0.003 mm to 0.005 mm, and 0.76 to 0.82, respectively. Among them, the ANN was the most accurate, while the Random Forest model was the least accurate.

- Increasing the dataset fraction led to a steady improvement in all error metrics, though the rate of improvement diminished beyond approximately 75% of the data. While some models, particularly the neural networks, exhibited near-plateau behavior in MSE and R^2 after this point, others continued to show moderate gains, indicating that model sensitivity to dataset size varied.
- Among the tested techniques, CNN and ANN demonstrated superior performance and robustness across all dataset fractions, particularly when using smaller datasets, while the Random Forest model showed a higher sensitivity to limited datasets.
- ANN showed potential for the inverse problem of determining the required operating parameters to machine micro-channels with desired depth and width. When only the desired channel width and depth were used as inputs to the model, for the depth, the model achieved an MAE of approximately 0.034 mm, an MSE of approximately 0.002 mm^2, and an R^2 of 0.94. For width, an MAE of approximately 0.018 mm, an MSE of approximately 0.00067 mm^2, and an R^2 of 0.55 were achieved.
- For the inverse problem, when the full desired profile was used as input to the ANN, the model showed a reduced accuracy in predicting the depth, especially at higher aspect ratios, giving overall MAE of 0.015 mm, MSE of 0.002 mm^2 and R^2 of 0.77. This reduced accuracy could be attributed to the complexity and high dimensionality of the inputs which contained redundant information. The many-to-one mapping between inputs and outputs and the limited dataset size contributed to lowering the model's accuracy.

Acknowledgement

The authors gratefully acknowledge the financial support of the Natural Sciences and Engineering Research Council of Canada (NSERC Grant # RGPIN-2026-04550).

Declarations

Competing interest: The authors declare that they have no conflict of interest.

Data availability

The datasets analyzed during the current research are available at https://doi.org/10.5281/zenodo.17644983. The browser-based demonstrator of the forward and inverse predictors are available at https://asjm-channel-predictor.streamlit.app/.

References

[1] L. Giorleo, E. Ceretti, C. Giardini, Optimization of laser micromachining process for biomedical device fabrication, International Journal of Advanced Manufacturing Technology 82 (2016) 901–907. https://doi.org/10.1007/S00170-015-7450-2/METRICS.

[2] C. Guo, P. Koshy, F. Coelho, P.R. Selvaganapathy, Sink electrical discharge machining of hydrophobic surfaces, CIRP Annals 68 (2019) 185–188. https://doi.org/10.1016/J.CIRP.2019.04.101.

[3] J. Cai, J. Li, G. Liu, H. Luo, Y. Zhang, Study on ultrasonic transverse vibration assisted micro electrochemical machining of high aspect-ratio groove with controllable cross section, J. Manuf. Process. 141 (2025) 613–626. https://doi.org/10.1016/J.JMAPRO.2025.03.020.

[4] J.C. Aurich, B. Linke, M. Hauschild, M. Carrella, B. Kirsch, Sustainability of abrasive processes, CIRP Annals 62 (2013) 653–672. https://doi.org/10.1016/J.CIRP.2013.05.010.

[5] Y. Natarajan, K.L.N. Raj, P. Tandon, Measurement and analysis of pocket milling features in abrasive water jet machining of Ti-6Al-4V alloy, Archives of Civil and Mechanical Engineering 23 (2023) 1–16. https://doi.org/10.1007/S43452-022-00578-3/METRICS.

[6] M. Moghaddam, M. Papini, Topography prediction of high-aspect ratio features milled with overlapping abrasive slurry jet footprints considering fluid confinement effects, Int. J. Mach. Tools Manuf. 197 (2024) 104145. https://doi.org/10.1016/J.IJMACHTOOLS.2024.104145.

[7] K. Kowsari, H. Nouraei, B. Samareh, M. Papini, J.K. Spelt, CFD-aided prediction of the shape of abrasive slurry jet micro-machined channels in sintered ceramics, Ceram. Int. 42 (2016) 7030–7042. https://doi.org/10.1016/j.ceramint.2016.01.091.

[8] Y.I. Oka, K. Okamura, T. Yoshida, Practical estimation of erosion damage caused by solid particle impact: Part 1: Effects of impact parameters on a predictive equation, in: Wear, Elsevier, 2005: pp. 95–101. https://doi.org/10.1016/j.wear.2005.01.039.

[9] H. Nouraei, K. Kowsari, M. Papini, J.K. Spelt, Operating parameters to minimize feature size in abrasive slurry jet micro-machining, Precis. Eng. 44 (2016) 109–123. https://doi.org/10.1016/j.precisioneng.2015.10.008.

[10] D.A. Axinte, D.S. Srinivasu, J. Billingham, M. Cooper, Geometrical modelling of abrasive waterjet footprints: A study for 90° jet impact angle, CIRP Ann. Manuf. Technol. 59 (2010) 341–346. https://doi.org/10.1016/j.cirp.2010.03.112.

[11] M.C. Kong, S. Anwar, J. Billingham, D.A. Axinte, Mathematical modelling of abrasive waterjet footprints for arbitrarily moving jets: Part i - Single straight paths, Int. J. Mach. Tools Manuf. 53 (2012) 58–68. https://doi.org/10.1016/j.ijmachtools.2011.09.010.

[12] M. Moghaddam, I. Hajiyev, M. Papini, Prediction and mechanism of surface evolution in high-pressure slurry jet micro-machining of channels, Precis. Eng. 82 (2023) 251–269. https://doi.org/10.1016/J.PRECISIONENG.2023.04.003.

[13] M. Moghaddam, P. Di Giorgio, M. Papini, Modeling eroded topography in masked abrasive slurry jet pocket milling, Int. J. Mech. Sci. 285 (2025) 109830. https://doi.org/10.1016/J.IJMECSCI.2024.109830.

[14] P. Ramesh, K. Mani, Prediction of surface roughness using machine learning approach for abrasive waterjet milling of alumina ceramic, International Journal of Advanced Manufacturing Technology 119 (2022) 503–516. https://doi.org/10.1007/S00170-021-08052-9/METRICS.

[15] Ž. Ćojbašić, D. Petković, S. Shamshirband, C.W. Tong, S. Ch, P. Janković, N. Dučić, J. Baralić, Surface roughness prediction by extreme learning machine constructed with abrasive water jet, Precis. Eng. 43 (2016) 86–92. https://doi.org/10.1016/J.PRECISIONENG.2015.06.013.

[16] A. Nag, M. Gupta, N.S. Ross, D. Klichová, J. Petrů, G.M. Krolczyk, S. Hloch, Real-time prediction and classification of erosion crater characteristics in pulsating water jet machining of different materials with machine learning models, Archives of Civil and Mechanical Engineering 2024 24:2 24 (2024) 1–19. https://doi.org/10.1007/S43452-024-00908-7.

[17] Y.I. Mogul, I. Mogul, J.D. Quadros, M. Mohin, A. Aabid, M. Baig, M.A. Malik, Prediction of cutting depth in abrasive water jet machining of Ti-6AL-4V alloy using back propagation neural networks, Results in Engineering 25 (2025) 104520. https://doi.org/10.1016/J.RINENG.2025.104520.

[18] K. Ramesha, N. Santhosh, B.A. Praveena, B. Nagaraj, N.C.K. Naik, Q.N. Naveed, A. Lasisi, A.W. Wodajo, ANN and machine learning based predictions of MRR in AWSJ machining of CFRP composites, Scientific Reports 2025 15:1 15 (2025) 1–23. https://doi.org/10.1038/s41598-025-92602-8.

[19] R. Prabhu, M. Kanthababu, Prediction of surface roughness and depth of cut in abrasive waterjet milling of alumina ceramic using Machine learning algorithms, Expert Syst. Appl. 246 (2024) 123168. https://doi.org/10.1016/J.ESWA.2024.123168.

[20] R. V. Savangouder, J.C. Patra, S. Palanisamy, A Machine Learning Technique for Prediction of Cold Spray Additive Manufacturing Input Process Parameters to Achieve a Desired Spray Deposit Profile, IEEE Trans. Industr. Inform. 20 (2024) 12275–12283. https://doi.org/10.1109/TII.2024.3417300.

[21] M.R. Sookhak Lari, M. Papini, Inverse methods to gradient etch three-dimensional features with prescribed topographies using abrasive jet micro-machining: Part I – Modeling, Precis. Eng. 45 (2016) 272–284. https://doi.org/10.1016/J.PRECISIONENG.2016.03.004.

[22] A. Ghazavi, M. Papini, An inverse method for the abrasive jet micro-machining of high aspect ratio channels of desired topography – Part I, theory, Precis. Eng. 58 (2019) 57–69. https://doi.org/10.1016/J.PRECISIONENG.2019.05.003.

[23] A. Bilbao-Guillerna, D.A. Axinte, J. Billingham, G.B.J. Cadot, Waterjet and laser etching: the nonlinear inverse problem, R. Soc. Open Sci. 4 (2017). https://doi.org/10.1098/RSOS.161031.

[24] A. Ibrahim, M. Papini, Controlled depth micro-abrasive waterjet milling of aluminum oxide to fabricate micro-molds containing intersecting free-standing structures, Precis. Eng. 75 (2022) 24–36. https://doi.org/10.1016/j.precisioneng.2022.01.007.

[25] M.M. Nekahi, E.V. Vazquez, M. Papini, Numerical Simulation of Solid Particle Erosion of Alumina by Overlapping Irregular-Shaped Particle Impacts, Tribol. Lett. 70 (2022) 1–19. https://doi.org/10.1007/S11249-022-01591-6/FIGURES/19.

[26] N. Haghbin, F. Ahmadzadeh, J.K. Spelt, M. Papini, Effect of entrained air in abrasive water jet micro-machining: Reduction of channel width and waviness using slurry entrainment, Wear 344–345 (2015) 99–109. https://doi.org/10.1016/j.wear.2015.10.008.

[27] M. Teti, J.K. Spelt, M. Papini, Jet properties and mixing chamber flow in a high-pressure abrasive slurry jet: part II—machining rates and CFD modeling, International Journal of Advanced Manufacturing Technology 101 (2019) 3021–3034. https://doi.org/10.1007/s00170-018-3041-3.

[28] C. Chollet, Deep Learning with Python, 1st ed., Manning, 2017. https://www.manning.com/books/deep-learning-with-python (accessed November 5, 2025).

[29] I. Goodfellow, Y. Bengio, C. Courville, Deep Learning (Adaptive Computation and Machine Learning series), The MIT Press, 2016. https://www.deeplearningbook.org/ (accessed November 5, 2025).

[30] M.A. Nasiri, T. Dehbi, M. Papini, Abrasive slurry jet machining of maskless helical micro-channels on rods: Process modeling using computational fluid dynamics, Powder Technol. 464 (2025) 121196. https://doi.org/10.1016/J.POWTEC.2025.121196.

[31] H. Tang, J. Niu, H. Jin, S. Lin, D. Cui, Geometric structure design of passive label-free microfluidic systems for biological micro-object separation, (n.d.). https://doi.org/10.1038/s41378-022-00386-y.